Characterizing human α-1,6-fucosyltransferase (FUT8) substrate specificity and structural similarities with related fucosyltransferases

Received for publication, June 2, 2020, and in revised form, September 28, 2020 Published, Papers in Press, October 1, 2020, DOI 10.1074/jbc.RA120.014625

Bhargavi M. Boruah[1,‡], Renuka Kadirvelraj[2,‡], Lin Liu[1], Annapoorani Ramiah[1], Chao Li[3], Guanghui Zong[3], Gerlof P. Bosman[4], Jeong-Yeh Yang[1], Lai-Xi Wang[3], Geert-Jan Boons[1,4], Zachary A. Wood[2,*], and Kelley W. Moremen[1,2,*]

From the [1]Complex Carbohydrate Research Center and the [2]Department of Biochemistry and Molecular Biology, University of Georgia, Athens, Georgia USA, the [3]Department of Chemistry and Biochemistry, University of Maryland, College Park, Maryland USA, and the [4]Department of Chemical Biology and Drug Discovery, Utrecht Institute for Pharmaceutical Sciences, and Bijvoet Center for Biomolecular Research, Utrecht University, Utrecht, The Netherlands

Edited by Chris Whitfield

Mammalian Asn-linked glycans are extensively processed as they transit the secretory pathway to generate diverse glycans on cell surface and secreted glycoproteins. Additional modification of the glycan core by α-1,6-fucose addition to the innermost GlcNAc residue (core fucosylation) is catalyzed by an α-1,6-fucosyltransferase (FUT8). The importance of core fucosylation can be seen in the complex pathological phenotypes of FUT8 null mice, which display defects in cellular signaling, development, and subsequent neonatal lethality. Elevated core fucosylation has also been identified in several human cancers. However, the structural basis for FUT8 substrate specificity remains unknown.

Here, using various crystal structures of FUT8 in complex with a donor substrate analog, and with four distinct glycan acceptors, we identify the molecular basis for FUT8 specificity and activity. The ordering of three active site loops corresponds to an increased occupancy for bound GDP, suggesting an induced-fit folding of the donor-binding subsite. Structures of the various acceptor complexes were compared with kinetic data on FUT8 active site mutants and with specificity data from a library of glycan acceptors to reveal how binding site complementarity and steric hindrance can tune substrate affinity. The FUT8 structure was also compared with other known fucosyltransferases to identify conserved and divergent structural features for donor and acceptor recognition and catalysis. These data provide insights into the evolution of modular templates for donor and acceptor recognition among GT-B fold glycosyltransferases in the synthesis of diverse glycan structures in biological systems.

Glycan structures on cell surface and secreted glycoproteins contribute to numerous interactions with the extracellular environment (1–3). Nonreducing terminal glycan structures commonly serve as binding sites for protein interactions (4) and, in some instances, modifications to the glycan core structure can also modulate protein function by influencing interactions with binding partners or altering biological dynamics and function (5–17).

The contributions of fucose (Fuc) residues are unique among the various glycan epitopes that influence glycoprotein function (18). In mammalian cells, Fuc residues are found in four discrete contexts based on linkages to either peptide domains or glycan structures (18) and each is generated by a separate enzyme family that is distinguished by its CAZy classification (19). Fuc residues can be attached directly to Ser/Thr side chains on EGF or thrombospondin repeat domains through the action of POFUT1 (CAZY GT65) and POFUT2 (GT68), respectively (18, 20), which influence protein folding and quality control of the domains in the endoplasmic reticulum (designations here and below employ human gene terminology). Modifications of *N*- and *O*-glycoproteins and glycolipids with Fuc-α1,2-Gal linkages by FUT1 and FUT2 (GT11) can create H-antigens as precursors for ABO blood group structures (18, 21–23). Terminal Fuc-α1,3/4-GlcNAc linkages are generated by GT10 fucosyltransferases to form Lewis antigen structures important in immune and inflammatory responses and vertebrate development (24, 25). Finally, *N*-glycan structures can be modified by α1,6-Fuc addition to the innermost GlcNAc residue (core fucosylation) catalyzed by FUT8 (GT23) (18, 26–28). Two additional fucosyltransferase families have also been identified in nonmammalian systems (CAZy families GT37 and GT74 (29–31)). Structures for several of the FUT family members have been determined (20, 29, 30, 32–42) and all are GT-B fold catalytic domains (32, 43) comprised of two adjacent Rossmann-folds with active sites found in the cleft between the two domains.

The roles of core fucosylation by FUT8 are diverse. FUT8 gene disruption in mice causes postnatal semi-lethality with emphysema-like changes in the lungs and extracellular matrix destruction (44, 45), severe growth retardation (14), defects in antigen presentation and immune response (5), aberrant B-cell development (9), defects in T-cell receptor signaling (10, 46) impaired synaptic plasticity (47), schizophrenia-like symptoms (48), and enhanced neuroinflammation (49). Patients with FUT8-CDG harboring defects in the FUT8 gene also present a similar spectrum of clinical symptoms (50, 51).

This article contains supporting information.
‡These authors contributed equally to this work.
*For correspondence: Kelley Moremen, moremen@uga.edu; Zachary A. Wood, zaw@uga.edu.

An increase in core fucosylation has also been reported in numerous cancers (52–63) and secreted glycoprotein cancer biomarkers containing elevated core fucosylation have been developed (64–66). Numerous approaches for generation of nonfucosylated antibodies are also being pursued through glycoengineering to improve IgG-FcγR interactions as next-generation therapeutics (67, 68).

Given the high impact of core fucosylation in animal systems, we have pursued structural and kinetic studies to determine the molecular basis for substrate recognition and catalysis by FUT8. Numerous FUT8 substrate specificity studies have been performed (69–78), including substrate profiling with libraries of acceptor compounds and glycoprotein acceptors, but these studies only identified relative activities rather than performing detailed kinetic analysis (79–82). Kinetic studies were performed using a $GlcNAc_2$-$Man_3GlcNAc_2$-Asn (A2-Asn, see Fig. 2 for substrate nomenclature) glycan structure as acceptor (71), but the enzyme recognizes numerous additional *N*-glycan processing intermediates with varied affinities, which has resulted in conflicting data for some substrates (77, 78).

Initial structural studies on FUT8 over a decade ago determined the overall protein-fold (36), but the absence of bound ligands or substrates provided little insight into substrate recognition. Recently, structures were published for a FUT8–GDP–A2-Asn acceptor complex (41, 42) that identified many aspects of substrate recognition. In the present paper we describe several FUT8 structures, including complexes showing that the occupancy of GDP, a sugar donor analog, correlates with the ordering of specific loop regions important for an induced-fit conformation change upon donor binding. We also describe four glycan acceptor complexes that illustrate the structural basis for FUT8 substrate specificity and the roles of acceptor-binding site complementarity and steric hindrance in acceptor substrate selection. Detailed kinetic analysis using a library of glycan acceptors and a collection of FUT8 active site mutants identify the key interactions required for high affinity substrate recognition and catalysis. We also compare the FUT8 structure with several GT-B fucosyltransferases in other CAZy families to identify far more structural similarities between these enzymes than previously appreciated. Despite the strong structural similarities, each enzyme employs a different strategy for acceptor substrate recognition and catalysis. Overall, the data provide a framework for understanding the evolution of donor- and acceptor-binding template structures used by related fucosyltransferases, and by extension other GT-B fold enzymes, in selective substrate recognition and synthesis of diverse glycan structures in biological systems.

Results

Expression, purification, and enzymatic characterization of recombinant human FUT8

The soluble catalytic domain of human FUT8 was expressed as a secreted and N-terminally His-tagged GFP fusion protein in HEK293 cells as previously described for the production and biochemical characterization of numerous human glycosyltransferases (Fig. S1*A*) (83). Purification of the enzyme from the conditioned media, fusion tag cleavage, and further purification led to an enzyme preparation amenable to enzymatic and structural studies (Fig. S1*B*). The oligomeric structure of FUT8 was examined by size exclusion-multiangle light scattering (SEC-MALS) revealing a single peak eluting with a predicted molecular mass of ~132 kDa consistent with a predominately dimeric form for the ~62.6 kDa expression product with tags removed (Fig. S1*C*).

Enzymatic characterization of WT FUT8 with a library of glycan acceptors

Prior studies have focused on kinetic and inhibition studies using various donor substrates and analogs that profiled the contributions of the respective nucleoside, diphosphate, and sugar components (71). Acceptor specificities have also been profiled using a collection of *N*-glycoprotein (69, 75, 78), glycopeptide (72, 73, 75, 76, 84), and glycan-Asn substrates (71, 74, 78), or glycan arrays (41, 81) of acceptors, but analysis of acceptor kinetics has been restricted to fluorophore-tagged or glycopeptide-linked A2-Asn. Here, we have employed a panel of Asn-linked glycan substrates to assess activity and kinetic constants using GDP-Glo assays. Of the various substrates, the A1-Asn and A2-Asn substrates were shown to display the optimal catalytic efficiencies (k_{cat}/K_m) (Table S1 and Fig. 1), which is consistent with prior data demonstrating a requirement for the full GlcNAc-β1,2-Man-α1,3-Man- arm for high affinity substrate recognition (73). The K_m value for the A2-Asn substrate was higher (52 μM) than values previously reported for the fluorophore-tagged (12 μM (42)) or glycopeptide-linked A2-Asn (13 μM (71)) substrates consistent with the prior data indicating that extensions to the peptide backbone increases the affinity of the acceptor substrate (77, 78). The addition of a β1,4-GlcNAc residue to the GlcNAc-β1,2-Man-α1,3-Man arm (A3'-Asn) reduced catalytic efficiency by 4.1-fold (Fig. 1). Similarly, extension of the GlcNAc-β1,2-Man-α1,6-Man arm with a β1,4-Gal residue (G1-Asn) reduced catalytic efficiency by 4.8-fold, whereas additional branching to form A3-Asn or incomplete mannose trimming to form NM5N2-Asn reduced catalytic efficiency by 19.8- and 8.3-fold, respectively (Fig. 1). Substrates lacking the β1,2-GlcNAc on the Man-α1,3-Man arm (M5N2-Asn and M3N2-Asn intermediates) had drastically reduced catalytic efficiencies (1590-fold reduction and no detectable activity, respectively). Finally, a tetra-antennary substrate (A4-Asn) had no detectable activity as acceptor. These data, in combination with previous results on relative acceptor specificities (71, 73, 79–82), indicate that the unmodified GlcNAc-β1,2-Man-α1,3-Man arm in both A1-Asn and A2-Asn are the critical determinants for high affinity substrate recognition, and additional β1,4-GlcNAc branching (A3'-Asn) on the subterminal Man residues or modifications on the GlcNAc-β1,2-Man-α1,6-Man arm (A3-Asn, A4-Asn, NM5N2-Asn, or G1-Asn) interferes with acceptor recognition (Fig. 1). Thus, FUT8 acceptor specificity exhibits a stringent exclusion of substrates containing terminal glycan branching beyond the A2-Asn core structure.

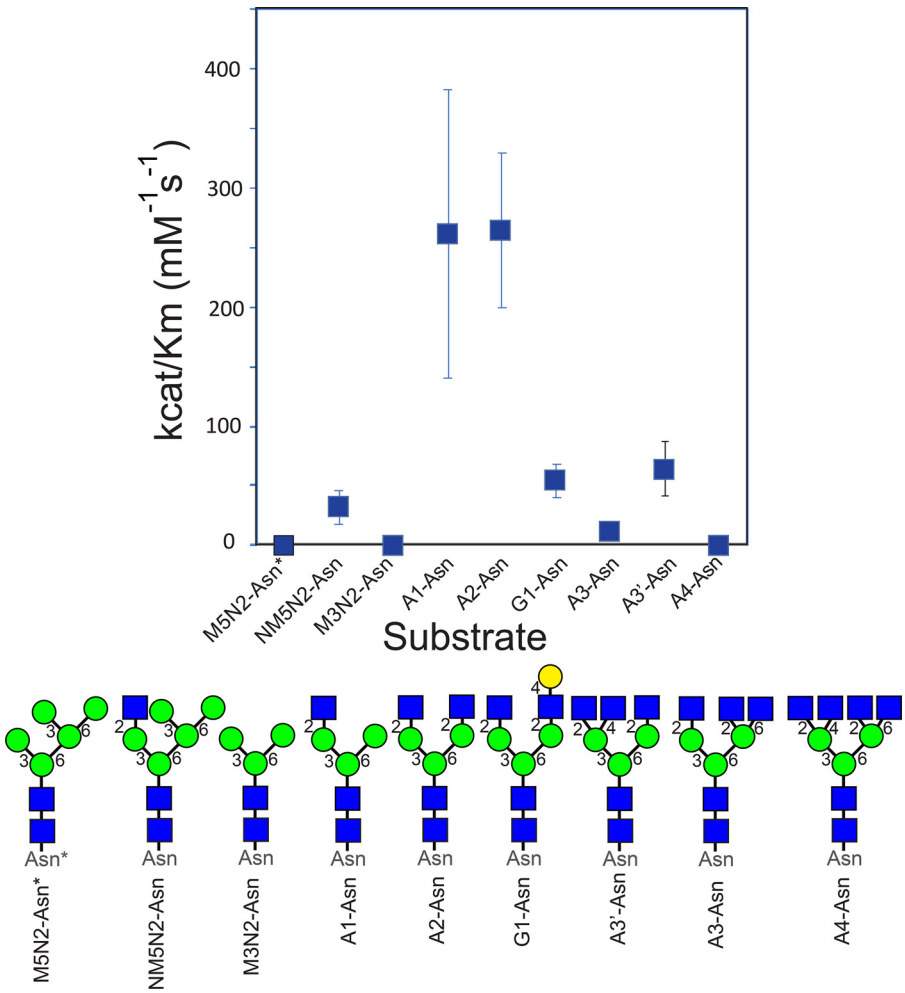

Figure 1. Enzymatic characterization of WT FUT8 with a library of glycan acceptors. The *upper panel* shows a graphical representation of of k_{cat}/K_m values for enzyme activity using WT FUT8 from Table S1 and the respective glycan acceptor structures shown in the *lower panel*. The nomenclature abbreviation is shown *below* each structure and the cartoon representations employ standard symbol nomenclature for glycans (116). *Asterisk* associated with the M5N2-Asn* structures indicates that this substrate contains an Fmoc modification (see "Experimental Procedures").

Crystallization and structure of the FUT8:GDP complex

Structural studies on FUT8 followed similar approaches that have been taken with other recent glycosyltransferase structures (32, 83, 85, 86) and other recent structures of human FUT8:A2-Asn complexes (41, 42). The soluble catalytic domain of FUT8 was initially crystallized in the presence of 5 mM GDP. X-ray diffraction data were collected to 2.25 Å resolution and the structure was solved by molecular replacement using the prior apo FUT8 structure (PDB 2DE0 (36)) as a search model. There were four chains in the asymmetric unit of the FUT8:GDP complex. The overall structure was comprised of a GT-B–fold but, as noted in the prior FUT8 structures (41, 42, 71), the enzyme has three large helical segments N-terminal to the GT-B–fold (two involved in homodimerization, see below) and an SH3 domain near the C terminus (Fig. 2).

Dimeric structure of FUT8

The SEC-MALS data for the purified enzyme indicated that FUT8 is a dimer in solution (Fig. S1). Similar to recent analysis of FUT8 structures (42, 87), the asymmetric unit of the present FUT8:GDP complex shows that chains B and C form a dimer with an interface that buries 3192 Å^2 of surface area (Fig. 2). Chains A and D form analogous dimers with their crystallographically related symmetry mates. PISA analysis indicates that the interface is stable, with a favorable solvation free-energy gain ($\Delta^i G$) of -29.8 kcal mol^{-1} and a p value of 0.057, which corresponds to a high likelihood that the surface is interaction-specific (88) The dimer interface is formed from the first two N-terminal α-helices of FUT8, which fold into a coiled-coil helix structure that associates with the corresponding coiled-coil pairs from adjacent subunits to form a 4-helix bundle, which buries heptad repeat residues in the hydrophobic core (Fig. 2, *A* and *B*) (89). Although this 4-helix bundle interaction was recognized in the recent FUT8:GDP:A2-Asn structures (41, 42, 87), it is notable that this dimer interface is also stabilized by extensive H-bonding and van der Waals interactions between the exposed face of the helical hairpin from one chain and the SH3 domain and residues from the GT-B–fold (residues 388-396) from the adjacent chain (Fig. 2*A*). Interestingly, the interactions between the SH3 domain and the lateral face of the 4-helix do not involve prolines, despite the fact the interface is formed from same loop regions that canonical SH3 domains

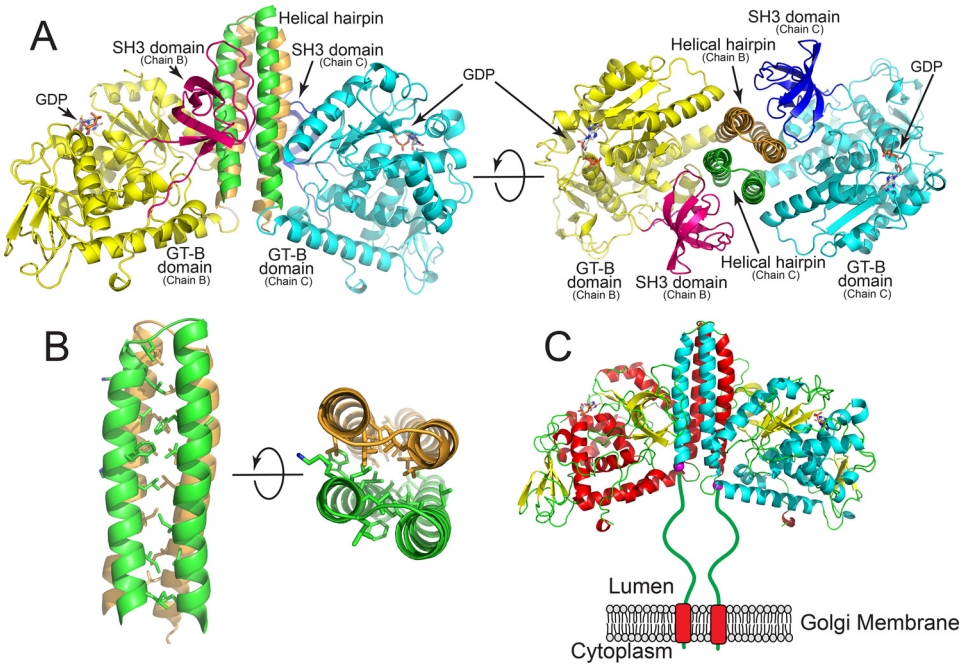

Figure 2. Structure of the FUT8:GDP complex. The structure of the human FUT8:GDP dimer. The interface is formed from an extended 4-helix bundle with contributions from two helices of each chain and likely represents the biological dimer in solution. *A,* representation of the homodimer where discrete domains of the proteins are colored differently. Chain B is comprised of an N-terminal helix pair (*tan*) followed by the GT-B domain (*yellow*), and the C-terminal SH3 domain (*magenta*). For chain C, the N-terminal helical pair (*green*) is followed by the GT-B domain (*cyan*) and the SH3 domain (*blue*). Two rotations of the structure are shown illustrating the 4-helix bundle and the interactions between the SH3 domains and the side of the helical bundle. *B,* zoom-in representation of hydrophobic side chain interactions within the 4-helix bundle shown as a side view and end-on view. *C,* cartoon representation of the full-length biological dimer of FUT8 as a transmembrane, Golgi-localized enzyme *in vivo* with a 77-amino acid linker "stem region" between the transmembrane span and the catalytic domain (*green line*). Helices of chain B (*red*) and chain C (*cyan*) are shown in cartoon representation, β strands are shown as *yellow cartoons* and GDP molecules are shown as *white sticks*. The N-terminal ends of the respective chains in the crystal structure are shown as *purple spheres*.

use to recognize proline-rich ligand sequences (90) (Fig. 2*A*). The N termini of the two chains are adjacent at the base of the 4-helix bundle, but ~77 amino acids of N-terminal "stem region" (91) were not resolved in the present structure and would be linked to the type 2 transmembrane segment in the full-length FUT8 enzyme (Fig. 2*C*). The program DISOPRED3 (92) predicts that the linker region of human FUT8 will most likely be intrinsically disordered.

GDP occupancy in the FUT8:GDP complex and the role of flexible loop conformations

Although the overall fold of the FUT8:GDP complex was similar to the prior apo structure (PDB 2DE0 (36)) and the recent FUT8:GDP:A2 complexes (41, 42), there were notable differences in conformations of several loops between each of the four chains in the GDP complex and also with the previously published structures. The loop regions are comprised of Loop 1 (residues 245-273), Loop 2 (residues 365-378), and Loop 3 (residues 436-443) (Fig. 3*B*). These three flexible loops enclose the GDP-binding subsite. Chains A and B of the FUT8:GDP complex contained unambiguous electron density for a well-ordered GDP, chain C contains a weakly ordered GDP, and chain D contains no density for the nucleotide (Fig. 3, *A* and *B*). The conformations and ordering of the three loops are strongly correlated with the occupancy of bound ligand. The fact that the crystals were grown in saturating GDP suggests that variable occupancy of the nucleotide is due to the crystal lattice selecting for loop conformations that weakened binding of the donor. Thus, in solution it is likely that these loops are flexible and undergo an induced fit folding upon binding of the donor substrate (Fig. 3*D*). The structures of each of the chains will be discussed separately below.

Chains A and B of the FUT8:GDP complex exhibit full occupancy for the bound GDP and Loops 1, 2, and 3 interact with the bound nucleotide (Fig. 3, *A* and *B*). The loop conformations of chain A are in analogous positions to the previously described FUT8:GDP:A2-Asn complexes (41, 42). Loop 2 harbors Arg^{365} and Lys^{369}, which have direct ionic interactions with the β-phosphate oxygen of the nucleotide and help to enclose the bound nucleotide (Fig. 4, *A* and *B*). Minor differences in Loop 2 conformations are seen between chains A and B and are likely due to crystal packing (Fig. 3*C*). Loop 3 adopts a single conformation in chains A and B, and contributes significant packing interactions to the nucleotide and ribose through Ala^{436} and Arg^{441}, respectively. In addition, Arg^{441} forms a complex ion pairing interaction with Asp^{368} in Loop 2, which in turn bridges to Arg^{365} in Loop 2 to completely enclose the bound nucleotide (the "Arg^{365}-Asp^{368}-Arg^{441} cage" (Fig. 4*C*). Finally, Tyr^{250} in Loop 1 forms an H-bond with the O2 ribose hydroxyl of the bound GDP in both chains A and B (Fig. 5, *A* and *B*). The β-phosphate has additional interactions with the side chain hydroxyl of Ser^{469} and the backbone nitrogen of Gln^{470}, whereas the α-phosphate has polar interactions with the backbone nitrogen atoms of Gly^{221} and Cys^{222}. The extensive electrostatic interactions with the β-phosphate likely explains why GDP is a much more potent inhibitor of FUT8

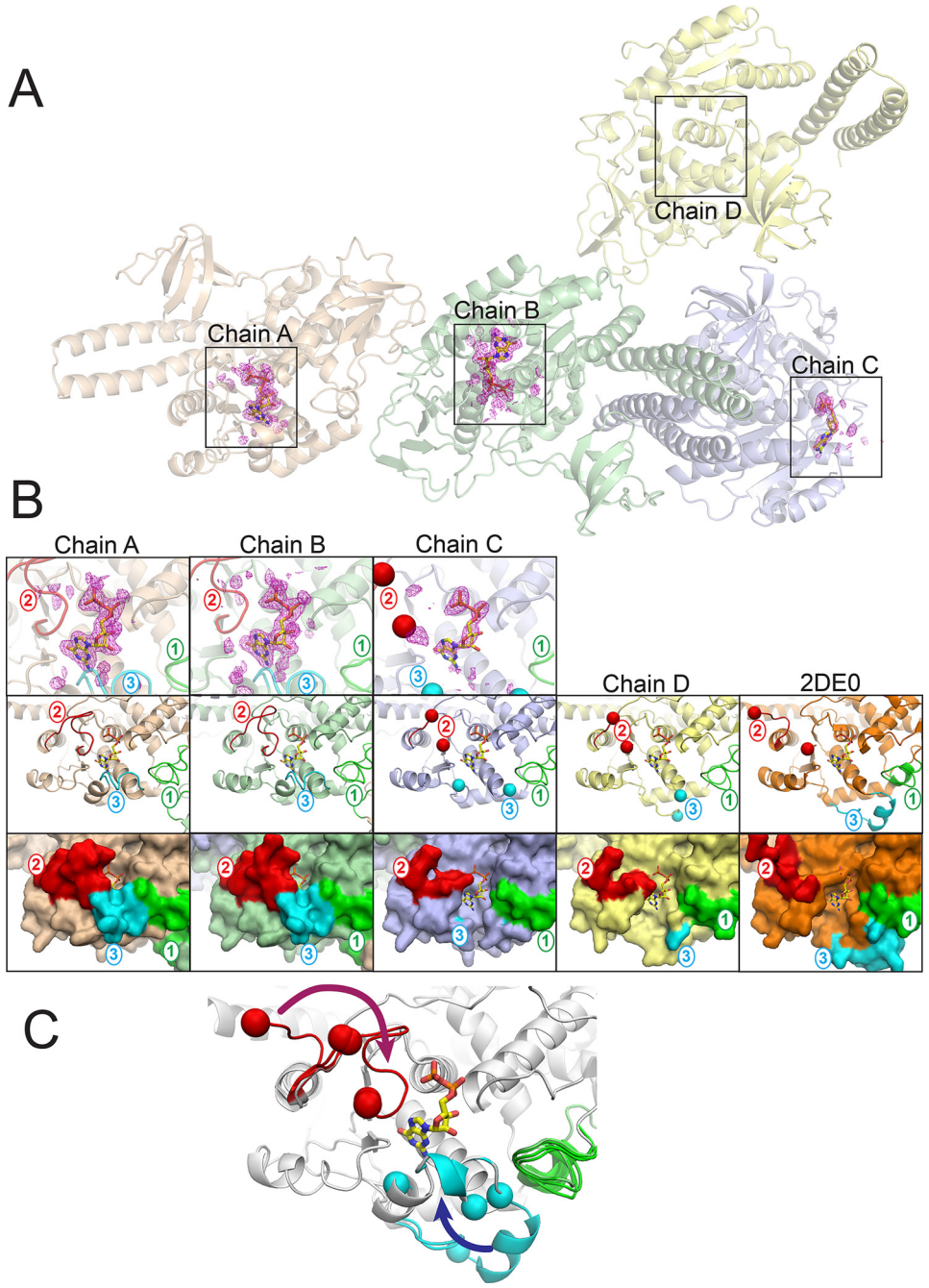

Figure 3. Varied structures and ligand occupancy between chains in the FUT8:GDP complex. The four chains in the FUT8:GDP asymmetric unit *A,* exhibited varied GDP occupancy between the respective chains and different loop conformations (chains A, B, C, and D in the crystal lattice are labeled and *boxed regions* represent the GDP-binding sites shown in *panel B*). Chains A and B show full occupancy of the bound GDP, whereas chain C shows partial occupancy, and chain D shows no occupancy as indicated by the difference density map ($F_o - Fc$) for the donor analog contoured at 3σ. *B,* zoom-in representations of the GDP-binding sites. *Upper panels,* zoom-in of the difference density maps ($F_o - F_c$) for the donor analog as indicated by the *boxed regions* in *panel A* with cartoon representations of the respective protein regions. *Middle panels,* chains A-D and the apo-FUT8 structure (PDB 2DE0 (36)) are shown in cartoon representation (chain A, *tan*; chain B, *green*; chain C, *slate*; chain D, *yellow;* Apo-FUT8 2DE0, *orange*). Significant differences in conformation were observed in three loops (Loop 1 (residues 245-273, *green*), Loop 2 (residues 365-378, *red*), and Loop 3 (residues 436-443, *cyan*)) with labels in the respective color. In chains C and D, disorder in Loops 2 and 3 were observed and the ends of the respective ordered regions are indicated by the *red* (Loop 2) or *cyan* (Loop 3) *spheres*, respectively. The 2DE0 structure also had a disordered region for Loop 2 indicated by the *red spheres*. GDP (*yellow* sticks) is modeled in the binding site of each chain for reference. *Lower panels,* surface representation of the four chains in FUT8:GDP and the apo-FUT8 (2DE0) structures with GDP (*yellow sticks*) modeled in the binding site of each chain for reference. Coloring is as shown in the *middle panels*. *C,* the progressive conformational changes in Loops 1-3 are illustrated by an overlay of the loops from chains A-D and the PDB 2DE0 structure. A fully extended "flipped-out" conformation is represented by the 2DE0 structure and progressive closure of Loop 2 and Loop 3 and repositioning of Loop 1 in chains C and D leads to partial occupancy in the GDP-binding site for chain C. Further closure of Loops 1-3 in chains A and B leads to full occupancy of the donor analog and completion of the induced fit donor interactions.

(3.6 μM K_i) than GMP (2.3 mM K_i) (71). The ribose O3 hydroxyl also H-bonds with the peptide nitrogen of Tyr^{220}, and the purine ring of the nucleoside interacts with His^{363}, Thr^{408}, and Asp^{453} (Fig. 4, *A* and *B*). There are additional minor differences in conformation for solvent-exposed side chains between chains A and B, but interactions with the bound GDP are conserved.

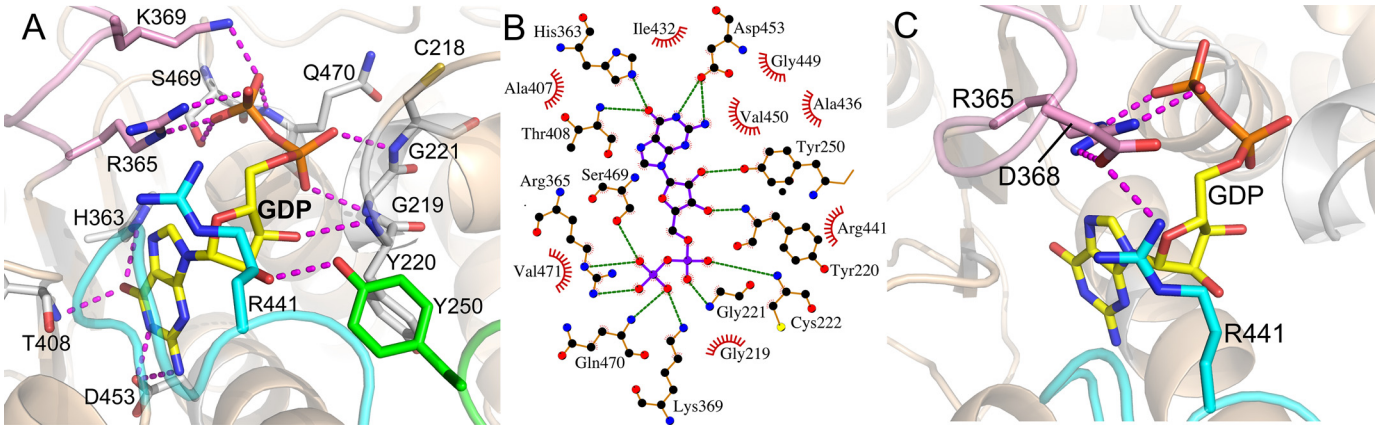

Figure 4. FUT8 interactions with GDP. Interactions between FUT8 and the GDP donor analog are illustrated in stick and cartoon representation (*A*) with hydrogen bonds indicated by *magenta dotted lines*. Interacting residues arising from Loop 2 are shown in *pink stick* representation, whereas residues coming from Loops 1 and 3 are shown as *green* and *cyan sticks*, respectively. *B*, Ligplot (117) representation depicting packing interactions (*red*, *feathered lines*) and hydrogen bonds (*green*, *dashed lines*) of GDP (highlighted in *yellow*) in the FUT8 active site (*orange ball and stick* with atomic colors). *C*, the Arg^{365}-Asp^{368}-Arg^{441} cage formed by the closing of Loops 2 and 3 to enclose the GDP-binding site results in a series of ionic interactions between Arg^{365} (Loop 2), Asp^{368} (Loop 2), and Arg^{441} (Loop 3). Only Arg^{365} directly interacts with the GDP (pair of ionic interactions with the β-phosphate), whereas the other two residues bridge Loops 2 and 3 to complete the enclosure of the donor nucleotide.

In contrast, chain C has significantly weaker electron density for the bound GDP (Fig. 3, *A* and *B*) and a significant portion of Loops 2 and 3 are completely disordered (indicated by *red* and *blue spheres* in Fig. 3*B*, *upper panels*). Only residues 365-366 and 375-376 are ordered in Loop 2 and residues 430-432 are ordered in Loop 3. The conformation of Loop 1 in chain C is similar to chains A and B with Tyr^{250} hydrogen bonding with the ribose O2 hydroxyl of the bound GDP. The disorder of Loops 2 and 3 opens the Arg^{365}-Asp^{368}-Arg^{441} cage and exposes the GDP to solvent (Fig. 3*B*). The rest of the binding site retains the other H-bonding and ionic interactions between the GDP and the polypeptide similar to chains A and B. Thus, the loss of the Arg^{365}-Asp^{368}-Arg^{441} cage and the associated electrostatic and packing interactions likely explains the lower occupancy of the nucleotide.

Chain D has no visible density for GDP in the binding site (Fig. 3, *A* and *B*). The disorder for Loop 2 was similar to chain C, but residues 430-435 in Loop 3 are positioned to indicate that this peptide segment is extended away from the GDP-binding site reminiscent of the position of the same loop in the PDB 2DE0 structure. A similar loss of binding residues is found for Loops 2 and 3 compared with chain C. In addition, Loop 1 in chain D is altered and does not position Tyr^{250} within H-bonding distance of the ribose O_2 hydroxyl in the nucleotide. Thus, loss of interactions with all three loops explains the absence of a bound GDP in chain D.

Finally, a comparison with PDB 2DE0 shows that the loops in the unliganded structure are similar in flexibility to those in chain D (Fig. 3*B*). In PDB 2DE0, Loop 2 extends away from the active site with residues 373-376 being disordered. Although Loop 3 is ordered in PDB 2DE0, it has moved >25 Å away from the GDP-binding site. The conformation of Loop 1 is similar to that observed in the FUT8:GDP chain D. These altered conformations are additional evidence that all three loops are likely disordered in solution, and supports an induced-fit folding upon nucleotide binding (Fig. 3*D*).

Structure of the FUT8:GDP:A2-Asn complex

To examine the acceptor substrate interactions, we crystallized a FUT8:GDP:A2-Asn complex. The structure was solved at 2.4 Å resolution in space group $P6_522$ with two chains in the asymmetric unit. Application of crystallographic symmetry reveals the same dimer that we previously observed. The two chains are essentially the same (rmsd 0.20 Å for 464 Cα atoms) with the exception of minor surface loops and solvent-exposed side chain differences. The structure is similar to chain A of the FUT8:GDP (rmsd 0.34 Å for 459 Cα atoms), with the exception that the conformation of Loop 2 is significantly different from the rest of the chains in the FUT8:GDP complex.

Both chains in the FUT8:GDP:A2-Asn complex display well-defined electron density for GDP and the entire A2-Asn molecule, which binds in a complementary surface groove on the face of the GT-B–fold and extends from a position adjacent to the GDP-binding site toward the SH3 domain (Fig. 5*A*). The FUT8:GDP:A2-Asn structure and its ligand interactions (Fig. 5, *B* and *C*) are essentially identical to those identified in the recently published FUT8:GDP:A2 complexes (41, 42) (the rmsd range from 0.45 to 0.54 Å for 450-467 corresponding Cα atoms in PDB 6TKV (41)). Briefly, GlcNAc residue ***N1*** (Fig. 5) is positioned adjacent to the GDP-binding site with the O6 hydroxyl facing toward the GDP ligand through H-bonding interactions with Glu^{373}. This residue is positioned in Loop 2 and is fully ordered in its interaction with the hydroxyl nucleophile of the acceptor. Glu^{373} also interacts through a salt bridge to Lys^{369} and subsequently to the β-phosphate oxygen of the GDP. These interactions suggest that Glu^{373} acts as the catalytic base to deprotonate the ***N1*** O6 nucleophilic hydroxyl and then in turn protonate the phosphate of the leaving GDP product (see "Catalytic Mechanism" below). Additional interactions include H-bonds from the ***N1*** O3 hydroxyl to Asp^{295} and Lys^{216}, the Asn amide nitrogen with Gly^{217}, and hydrogen bonds between Gln^{470} and the ***N2*** *N*-acetyl glycosidic oxygen. A further matrix of hydrogen bonding interactions extends throughout the length of the

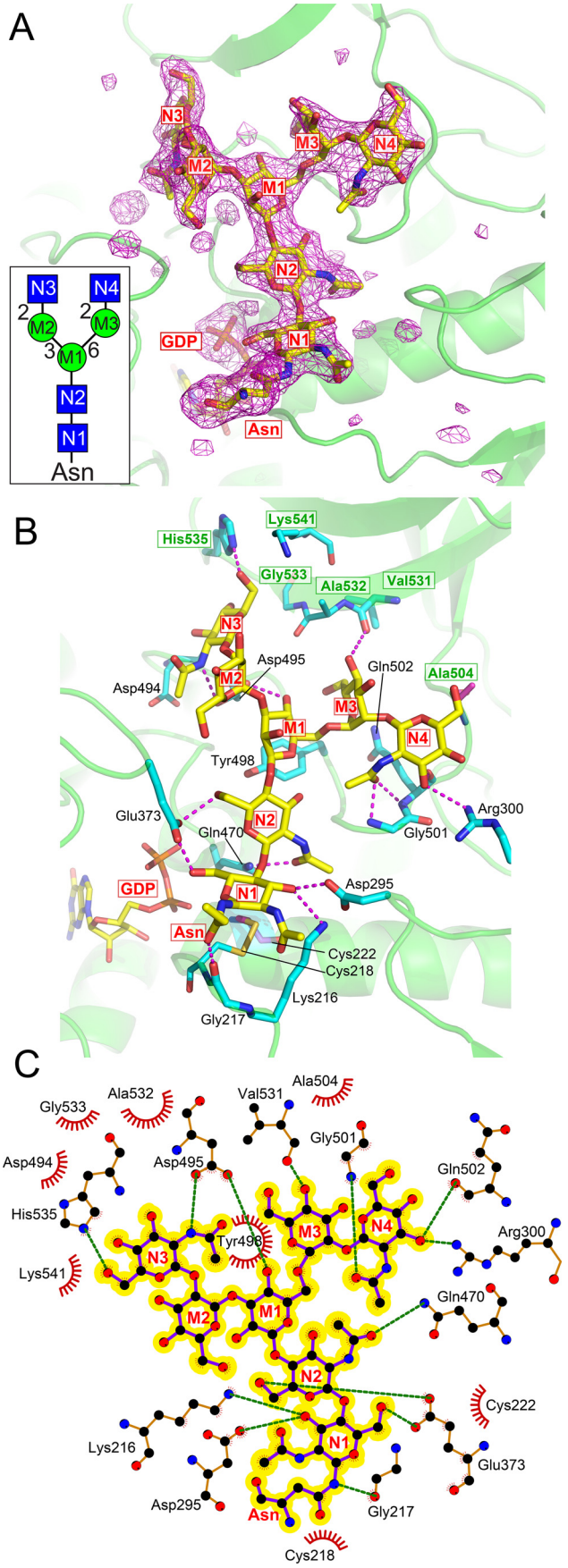

A2-Asn structure all the way to the nonreducing terminal GlcNAc residues (***N3*** and ***N4***). Many of the interactions with the terminal A2-Asn residues are contributed by the SH3 domain (Fig. 5*B*, *green* residue labeling with *green boxes*). All of the monosaccharides in the acceptor have at least one H-bond to the enzyme surface with the exception of the internal Man residue in the GlcNAc-β1,2-Man-α1,3-Man arm (***M2*** residue). The details of the acceptor interactions are shown in Fig. 5, *B* and *C*. Most notable among these interactions is the position of the SH3 domain, which sterically blocks the linear extension of the A2 glycan beyond the β-linked Man residue (***M1***) and leads to a bifurcation of the two terminal glycan branches in opposite directions across the surface of the SH3 domain. Each branch has interactions with the SH3 domain including residues ***N3***, ***M3***, and ***N4***. The close interaction of the ***M1*** residue with the SH3 domain surface also precludes binding of glycans containing a bisecting GlcNAc residue.

Enzymatic characterization of FUT8 active site mutants

To confirm the contributions of binding site amino acids to acceptor glycan interactions we mutated each of the respective amino acids to alanine, tested the activity, and performed kinetic analysis on the active mutants (Fig. 6*C*). A subset of the residues in the GDP-binding site had previously been tested for enzyme activity (36) and we confirmed that mutation of these and other residues that directly interact with the GDP lead to complete enzyme inactivation (Table S3 and Fig. 6, *B* and *C*). In addition, we probed residues that contribute to acceptor glycan interactions and found that mutation of three residues, Asp^{295} that H-bonds with the O3 hydroxyl of ***N1***, Tyr^{498} that provides van der Waals packing interactions with the hydrophobic face of the β-Man residue (***M1***), and Asp^{495} that H-bonds with ***M1*** and the terminal ***N3*** residue, all lead to complete loss of enzyme activity (Fig. 6*A*). Mutations of other interacting residues result in significantly decreased catalytic efficiency, but not complete inactivation (Fig. 6*C*). These reductions in k_{cat}/K_m include Lys^{216} that H-bonds with ***N1*** (160-fold reduction in k_{cat}/K_m), Gln^{470} that H-bonds with ***N2*** (80-fold reduction), Asp^{494} adjacent to ***N3*** (800-fold reduction), His^{535} that H-bonds with ***N3*** (11-fold reduction), and Gln^{502} that H-bonds with ***N4*** (16-fold reduction). A similar reduction in activity was previously seen for mutants in the SH3 domain including H535A as well as H535A/Lys541A and T550A/L552A double mutants in prior studies (93) and a collection of residues conserved between

Figure 5. FUT8 interactions with the A2 acceptor. *A*, the structure of the FUT8:A2-Asn acceptor complex is shown as a difference density map ($F_o - F_c$) of the acceptor contoured at 3.5 σ before modeling the $GlcNAc_2Man_3GlcNAc_2$-Asn structure (*yellow sticks*). The *inset* shows a cartoon representation (see Fig. 2 for cartoon nomenclature) of the A2-Asn glycan with labeling of each monosaccharide inside each respective symbol and the corresponding labeling is also employed in the density map. *B*, the FUT8:A2-Asn complex is shown in *yellow stick* and cartoon representation with interacting residues shown in *cyan stick* representation and hydrogen bonds as *magenta dashed lines*. Monosaccharide residues of the A2-Asn structure are labeled as in *Panel A*. GDP is shown in *yellow stick* representation. Residues arising from the SH3 domain are indicated by *green* residue labeling enclosed in *green boxes*. *C*, Ligplot (117) representation depicting packing interactions (*red, feathered lines*) and hydrogen bonds (*green, dashed lines*) of A2-Asn (highlighted in *yellow*) in the FUT8 active site (*orange ball and stick* with atomic colors).

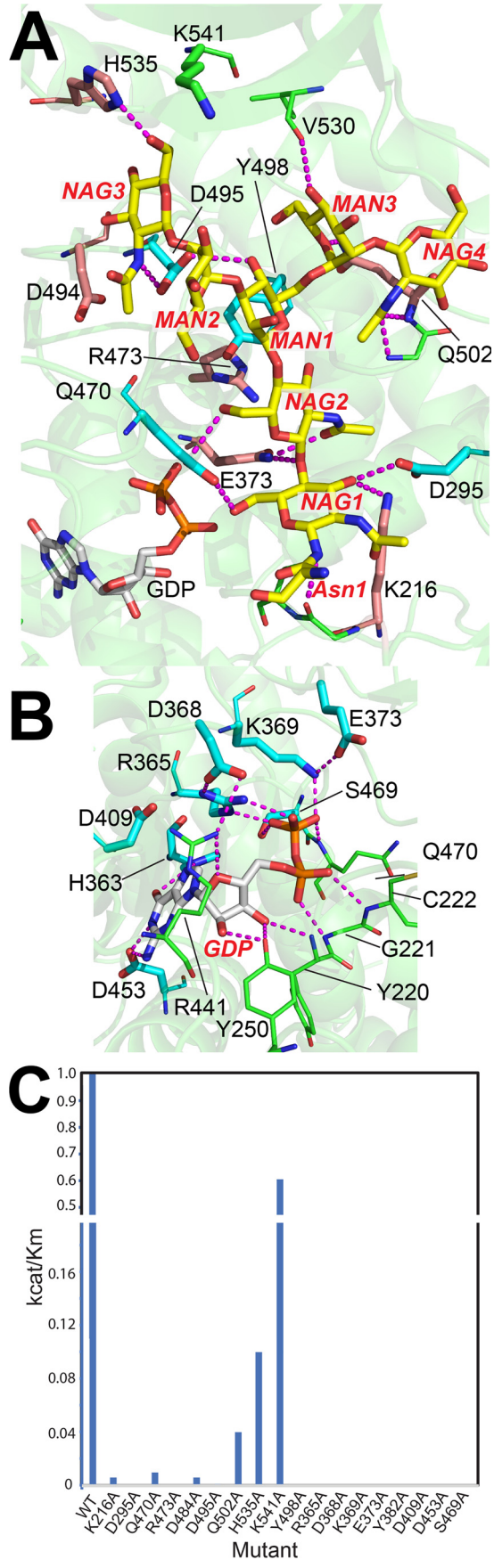

human FUT8 and chicken c-Src (87) demonstrating the critical role of the SH3 domain in providing acceptor substrate specificity and affinity. Thus, whereas the donor-binding site is exceptionally sensitive to mutational perturbation, the acceptor-binding site has fixed points of essential interaction and other regions that contribute incremental binding energy to catalytic efficiency.

Structures of FUT8:GDP:A3′-Asn FUT8:GDP:A3-Asn, FUT8:GDP:NM5N2-Asn complexes and implications for recognition of alternative substrates

The kinetic studies with varied acceptor substrate structures indicated a preference for glycans containing an unmodified GlcNAc-β1,2-Man-α1,3-Man arm (A1-Asn and A2-Asn structures), and reduced activities for substrates that harbor additional modifications to the core A2-Asn structure. The impacts of these modifications on k_{cat}/K_m are highlighted in Fig. 7*A*. To examine substrate interactions with alternative acceptor structures we performed additional co-crystallization studies with A3′-Asn (Fig. 7*B*), A3-Asn (Fig. 7*C*), and NM5N2-Asn (Fig. 7*D*) acceptors. In each case we obtained well-defined electron density for at least a portion of the corresponding acceptor glycan.

The structure of the FUT8:GDP:A3′-Asn complex was solved at 3.3 Å resolution, in the same space group as FUT8:GDP:A2-Asn. FUT8:GDP:A3′-Asn has two chains in the asymmetric unit and both chains display unambiguous electron density for the GDP and for all residues of the A3′-Asn acceptor. The overall enzyme structure was similar to the two chains of the FUT8:GDP:A2-Asn complex (rmsd 0.22-0.29 Å for 465 Cα atoms between the corresponding chains) and the donor and acceptor interactions within the respective binding subsites were identical to the FUT8:GDP:A2-Asn complex. The major difference was the presence of an extra β1,4-GlcNAc residue (***N5***) on the GlcNAc-β1,2-Man-α1,3-Man arm that distinguishes the A3′-Asn structure from A2-Asn (Fig. 7*B* and *inset*). In both chains, the ***N5*** residue faces into the solvent and does not contribute directly to acceptor-binding interactions.

The structure of the FUT8:GDP:A3-Asn complex was determined at 2.47 Å resolution in space group $P6_5$ with eight chains in the asymmetric unit. All eight chains display unambiguous electron density for the GDP, but density for the acceptor was evident only in chains A, D, E, and H. In each case where the acceptor density was present, only a single distal arm and the core of the glycan structure (GlcNAc-β1,2-Man-α1,3-Man-β1,4-GlcNAc-β1,4-GlcNAc-β-Asn) was resolved (Fig. 7*C*). The Man-α1,6- (***M3***) branching residue from the core β-Man (***M1***) was disordered along with the two distal GlcNAc residues (***N4*** and ***N6***) extending from this arm (Fig. 7*C* and *inset*). The disorder for these three monosaccharides in the acceptor

Figure 6. Structural representation of the FUT8 active site mutants depicting the effects on enzyme kinetics. Residues in the FUT8 acceptor-binding site (*A*) or donor site (*B*) were mutated to Ala, expressed, purified, and assayed for enzyme activity using the A2-Asn acceptor substrate (Table S3). *C*, k_{cat}/K_m values for each of the respective mutants are shown. In *A* and *B*, residues that led to enzyme inactivation when mutated to Ala are indicated by *cyan stick* representations. Residues that reduced activity are indicated by *tan stick* representation. The K541A mutation had a minor impact on k_{cat}/K_m and is indicated in *green stick* representation.

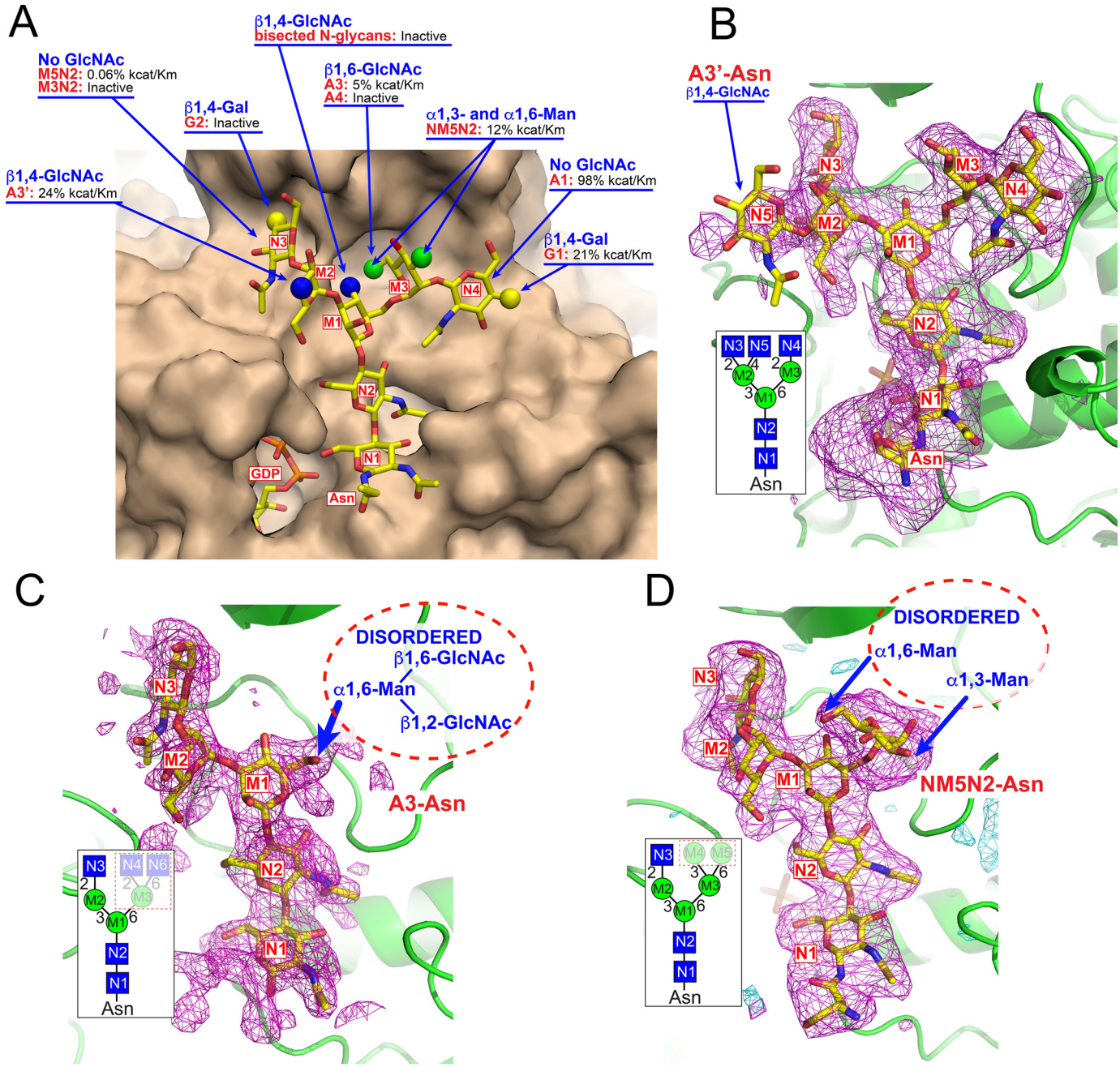

Figure 7. Impact of acceptor modifications on enzyme activity and structures of acceptor complexes. Modifications to the acceptor glycan structure impacts catalytic efficiency in enzyme assays (*A*). Surface representation of the FUT8:A2-Asn complex (*tan*) with the A2-Asn structure are displayed in *yellow stick* representation. Alternative acceptor structures are indicated by spherical representations at positions where they differ from the A2-Asn structure. For each modification, the respective glycan structure is shown in *red* text and the effect on enzyme activity is listed based on enzyme assay data from Table S1. In cases where the respective acceptor was listed as "inactive" there was no activity detected in the *in vitro* enzyme assays. Values for k_{cat}/K_m are listed by comparison to activity using the A2-Asn substrate. The lack of activity toward the G2-Asn substrate or the glycans with bisected GlcNAcs were based on prior assays from other groups (73, 75, 82). The Polder maps (115) (*magenta mesh* and contoured at 2.8 σ and 3.5 σ, respectively) were obtained from the crystal structures of three additional acceptor complexes and are shown in *B–D*. The Polder maps (115) for A3′-Asn, A3-Asn, and NM5N2-Asn acceptors were calculated following a modified procedure to reduce model bias (see "Experimental procedures"). *B*, the structure of the FUT8:GDP:A3′-Asn complex was essentially the same as the FUT8:GDP:A2-Asn complex except for the additional β1,4-GlcNAc residue (***N5***) extending from the Man-α1,3- residue (***M2***). This residue extends into the solvent and has no additional interactions with the enzyme surface. The *inset* in *B* indicates the cartoon representation of the A3′-Asn glycan with residue labeling that is also used to label the residues in the difference density (Polder) map. *C*, the structure of the FUT8:GDP:A3-Asn complex retained the density for the GlcNAc-β1,2Man-α1,3Man-β1,4GlcNAc-β1,4GlcNAc-βAsn region of the A2-Asn complex. However, the entire extension from the Man-α1,6- arm (residues M3, N4, and N6) was disordered and not resolved in the structure (*whited out region* in the *dotted box for the inset*; structure and *dotted oval* in the Polder map (115)). *D*, the structure of the FUT8:GDP:NM5N2-Asn complex also retained the electron density for the GlcNAc-β1,2Man-α1,3Man-β1,4GlcNAc-β1,4GlcNAc-βAsn region similar to the A2-Asn complex along with density for the Man-α1,6- (***M3***) residue extending from the Man-β1,4- residue (***M1***). However, the additional terminal Man-α1,3- (***M4***) and Man-α1,6- (***M5***) residues in the NM5N2-Asn structure were disordered and not resolved in the structure (*whited out region in dotted box* for the *inset* structure and *dotted oval* in the Polder map (115)).

complex indicates that the predicted steric hindrance (Fig. 7*A*) for the additional β1,6-GlcNAc residue (***N6***) altered the positioning of the entire branch.

The structure of the FUT8:GDP:NM5N2-Asn complex was determined at 3.2 Å resolution. Similar to FUT8:GDP:A3-Asn, this structure was also in space group $P6_5$ with eight chains in the asymmetric unit. For this complex, the electron density for both the GDP and the GlcNAc-β1,2-Man-α1,3-[Man-α1,6-]Man-β1,4-GlcNAc-β1,4-GlcNAc-Asn portion of the acceptor was visible in all eight chains, although the order of the GlcNAc-Asn region of the acceptor varied between chains (Fig. 7*D* and *inset*). The electron density for the ***M3*** branch extending from the core β-Man (***M1***) is well-defined. However, density for the ***M4*** and ***M5*** residues was weak and they were left unmodeled.

The steric constraints of the acceptor-binding site clearly indicate that the 1,6-substituents on the ***M3*** residue in the A3-Asn and NM5N2:Asn complexes are not compatible with the same binding geometry as the A2-Asn structure (GlcNAc-β1,6- (***N6***) for A3-Asn and Man-α1,6- (***M5***) for NM5N2-Asn). These modifications to the ***M3*** residue lead to rotation or disorder of the more flexible Man-α1,6- linkage between ***M3*** and ***M1*** to accommodate the bulky branched substituents and likely account for the reduced catalytic efficiencies for these glycan acceptors.

Sequence and structural alignment of FUT8 with other related GTs

Previous sequence (94), HCA (95), and structural (42) alignments of fucosyltransferases have compared α-1,2- and α-1,6-fucosyltransferases with mammalian protein-*O*-fucosyltransferases (POFUTs) and identified three conserved sequence motifs that are common among the sequence families (Fig. S2, *red boxes*), including residues involved in binding the nucleotide portion of the sugar donor (42). Structures are now available for mouse (38), human (37), and *Caenorhabditis elegans* (33) POFUT1 (GT), *C. elegans* (39), and human (40) POFUT2 (GT68), *Arabidopsis* FUT1 (GT37 (29, 30)), NodZ (GT23, (35, 96)), and human FUT8 (GT28) and structural alignment using the PROMALS3D server (97) allowed us to make a more comprehensive comparison between these enzymes to identify additional conserved structural elements. The resulting alignment revealed extensive structural similarity far beyond the three previously identified motifs (Fig. S2, *blue boxes*). Visualization of these conserved elements (Fig. S3*A*, *Conserved*) indicated the core of both Rossmann-folds were highly conserved among these enzymes including more than eight helical segments and four of the β-strands within the Rossmann-fold associated with the donor-binding site. Six β-strands of the second Rossmann-fold are less conserved in position, but still maintain a high degree of structural similarity among the collection of enzymes (Fig. S3, *A* and *B*). The degree of structural similarity is striking considering pairwise primary sequence similarities were <15%. The PROMALS3D alignment also identified 13 amino acids that are most conserved among the structures, some of which were noted in a more focused comparative analysis of the sugar donor-binding site (42). Displaying these amino acids within the framework of the FUT8 structure shows that 9 of the 13 amino acids are clustered within the base of the GDP-binding site proximal to the Rossmann-fold (Fig. S3*C*) and either directly interact with the donor or contribute to the architecture of the donor site. The other four residues are distributed more widely within the FUT8 structure and do not interact with substrates or contribute to catalysis. For FUT8, the conserved binding site residues are not a part of Loops 1-3 that undergo conformational changes upon donor binding and, surprisingly, these three dynamic loops are not conserved in position or sequence among the other fucosyltransferase structures.

In contrast to the similarity in the underlying Rossmann-fold and donor-binding subsite, each of the enzymes are entirely different in their modes of interactions with their respective acceptor molecules (Fig. S3). Although the positions of acceptor interactions are approximately similar in the clefts between the two Rossmann-folds, each enzyme employs unique loop insertions into the Rossmann-fold scaffold to assemble the acceptor binding subsites (Fig. S3). For the POFUTs that recognize larger protein domain structures, the interactions are assembled through the generation of a deep cleft between the two subdomains. For the glycan-directed fucosyltransferases (FUT8 and AtFUT1), the interactions are through a more flattened face of the cleft and, for FUT8, the recruitment of an additional SH3 domain insertion near the C terminus. This clearly indicates the presence of evolutionary divergence in the respective loop regions to provide unique acceptor binding specificities, whereas the core scaffold of the GT-B structure and donor interactions are more conserved.

An even more striking observation from the aligned structures is the similarities in positions for the acceptor nucleophiles in the respective structures (Fig. 8*B*). FUT8 and AtFUT1 (29, 30) structures have been solved as extended glycan acceptor complexes, whereas POFUT1 (38) and POFUT2 (39) have been solved in complex with EGF and thrombospondin repeat domain acceptors, respectively. In each instance, the corresponding acceptor hydroxyl has been identified in a position for nucleophilic attack. Surprisingly, despite the differences in the respective acceptor structures, the nucleophilic hydroxyls are positioned similarly. The nucleophilic hydroxyls for the two glycan-directed enzymes (FUT8 and AtFUT1) superimpose almost exactly. Similarly, the nucleophilic Ser/Thr hydroxyls for the POFUTs also superimpose with each other at a position <2 Å from the nucleophiles for the glycan-directed enzymes.

FUT8 catalytic mechanism

Among the six aligned fucosyltransferases in Fig. S3, only two have a clearly identified catalytic base (FUT8 and POFUT2 (39)). POFUT1 and AtFUT1 have no apparent ionizable side chain in proximity to the acceptor hydroxyl and are proposed to use a S_N1 mechanism employing a proton shuttle (20, 30, 33, 38). NodZ was not solved as an acceptor complex and its catalytic base was not identified (35, 96).

To identify the catalytic mechanism of FUT8 we superimposed the aligned structure of the intact GDP-Fuc from the POFUT2:GDP-Fuc complex (40) in the donor-binding site (Fig. 8*A*). This resulted in the placement of the Fuc residue in the

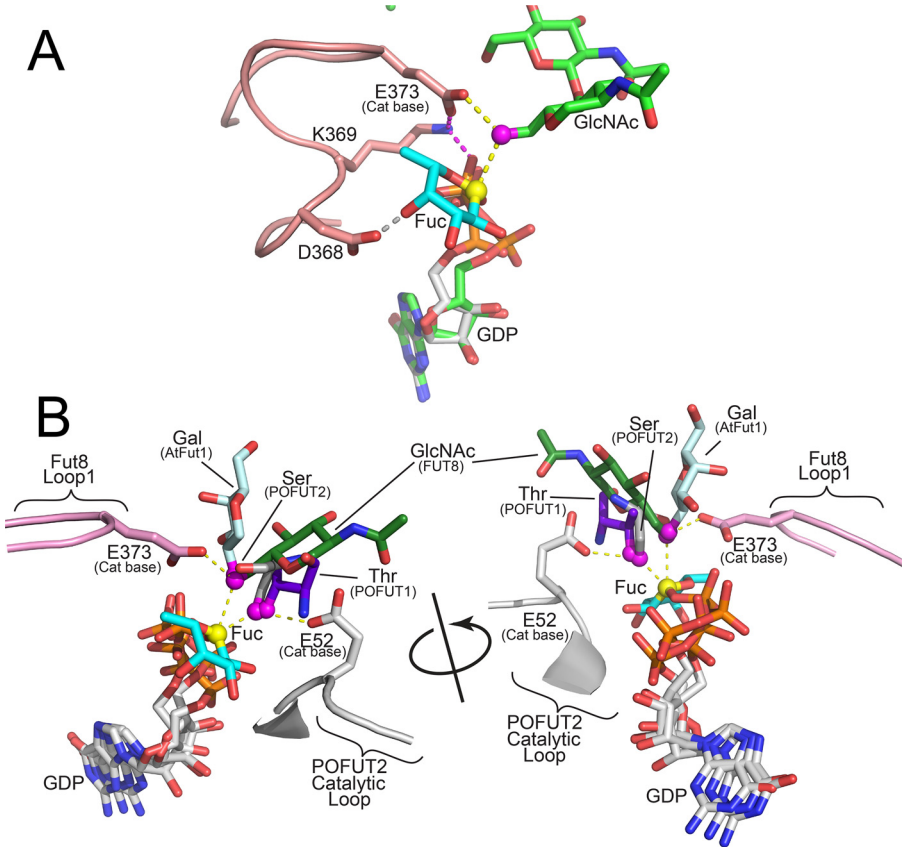

Figure 8. Proposed catalytic mechanism of FUT8 and other fucosyltransferases. *A,* the proposed mechanism for FUT8 is illustrated based on the alignment of the FUT8:GDP:A2-Asn complex with the human POFUT2:GDP-Fuc complex (PDB 4AP6 (40)). The aligned structures overlay the nucleotide and ribose (*green* sticks for GDP bound to FUT8 and *white sticks* for GDP-Fuc bound to POFUT2) in both structures and place the Fuc (*cyan sticks*) residue within the FUT8 active site in an appropriate position for an in-line S_N2 inverting mechanism. The O6 GlcNAc nucleophile (*magenta sphere*) in the A2-Asn acceptor (*green sticks*) is positioned appropriately relative to the Fuc C1 (*yellow sphere*) and the Glu^{373} catalytic base (*pink sticks*). The trajectory for the catalytic base and nucleophilic attack is shown with *yellow dotted lines*. The Glu^{373} base is also in proximity to Lys^{369} in Loop 2 (*pink* cartoon), which shuttles the proton from Glu^{373} to the β-phosphate of the GDP leaving group (*magenta dotted lines*). The position of the GlcNAc is also stabilized by an H-bond between O4 and Asp^{368} in Loop 2 (*gray dotted line*). *B,* the structures FUT8:GDP:A2-Asn, POFUT1:GDP-Fuc:EGF domain complex, *C. elegans* POFUT2:GDP:thrombospondin repeat complex, human POFUT2:GDP-Fuc complex, NodZ:GDP complex, and *Arabidopsis* FUT1:GDP–xylo-oligosaccahride complex were aligned as described in Fig. S3. The acceptor monosaccharide residues for the respective glycans (FUT8 (*green sticks*) and AtFUT1 (*light blue sticks*)) or protein domains (POFUT1 (*purple sticks*) and POFUT2 (*gray sticks*)) are shown as single monosaccharides or amino acids (full Ser side chain modeled for mouse Factor VII EGF1 domain from an mutant Ala residue in the mouse POFUT1:GDP-Fuc:EGF domain structure (38)). The respective hydroxyl nucleophiles are shown as *magenta spheres*. The donor analogs (GDP for all structures except POFUT1) are shown in *white stick* representation. The GDP-Fuc structure from the POFUT1:GDP-Fuc complex is shown in *white stick* representation except for the Fuc residue, which is shown as *cyan sticks* with C1 as a *yellow sphere*. The proposed catalytic base for FUT8 (Glu^{373} in Loop 2) is shown in *pink stick* representation. *Yellow dotted lines* represent the deprotonation trajectory of the nucleophilic hydroxyl by Glu^{373} and the subsequent S_N2 nucleophilic attack of the GDP-Fuc sugar donor as proposed in the FUT8 catalytic mechanism. The proposed catalytic base for POFUT2 (*E52*) is shown in *white stick* representation. *Yellow dotted lines* represent the deprotonation trajectory of the nucleophilic Ser hydroxyl by Glu^{52} and the subsequent S_N2 nucleophilic attack of the GDP-Fuc sugar donor in the POFUT2 catalytic mechanism. The two catalytic bases interact from the opposite faces of their respective nucleophilic hydroxyls and emerge from completely different regions of the conserved core structures of their respective enzymes.

FUT8 active site without steric hindrance and predicted H-bonds for the fucose O2 with the backbone nitrogen of Gly^{219} and for O4 with Asp^{368} (from Loop 2). This latter interaction is consistent with the loss of FUT8 activity for the D368A mutant (Table S3). In addition, C1 of the Fuc residue is directly in line for nucleophilic attack by the O6 hydroxyl of ***N1*** (Fig. 8*A*). Thus, the structure of the FUT8:GDP:A2-Asn complex and the modeled donor confirm the inverting catalytic mechanism of the base-catalyzed S_N2 nucleophilic attack of the sugar nucleotide donor by the ***N1*** O6 hydroxyl.

Although both FUT8 and POFUT2 perform similar S_N2 in-line nucleophilic attacks of their respective GDP-Fuc donors, the catalytic base for POFUT2 (E52 (39)) originates from a completely different region of the protein structure compared with FUT8 (Fig. 8*B*). The catalytic base (Glu^{373}) for FUT8 is on the opposite side of its acceptor nucleophile relative to Glu^{52} in POFUT2, whereas POFUT1 and AtFUT1 do not have ionizable side chains at either position. Clearly, whereas the enzymes conserve residues for donor and nucleophile binding, the constraints for positioning the catalytic base and enzymatic mechanism are not conserved among these enzymes.

Discussion

Prior studies on FUT8 examined the range of glycan substrates that can be recognized (69–78) and how these modifications modulate a diverse array of biological functions (6, 8–10, 12, 14, 15, 17, 44–68, 98, 99). Our detailed kinetic analysis demonstrates the importance of the *N*-glycan GlcNAc-β1,2-Man-α1,3-Man arm as a key determinant for high affinity substrate recognition. Glycans that have not been modified by MGAT1

(*e.g.* $Man_{5\text{-}3}N_2$-Asn) were ineffective substrates for human FUT8 even though recombinant expression data previously indicated these structures can be modified when mannose trimming is inhibited or FUT8 has been overexpressed (77, 78, 100). The A1-Asn and A2-Asn processing intermediates exhibited the highest catalytic efficiencies, while A3'-Asn, A3-Asn, G1, or incomplete processing to NM5N2-Asn significantly reduced catalytic efficiency, and extension to A4-Asn abolished activity (Fig. 7*A*). Thus, FUT8 exhibits a highly constrained active site that restricts steric access to all but a few structures despite the fact that all *N*-glycan processing intermediates contain the same core Man_3-$GlcNAc_2$-Asn acceptor structure.

Structures of FUT8 donor complexes

To address the restricted substrate recognition, we first examined structures of FUT8 in complex with the donor analog, GDP. Loop regions were identified that were extended away from the donor-binding site when no GDP was bound and a progressive increase in GDP density was found as the loops flipped in to enclose the donor analog. Thus, catalysis proceeds by initial GDP-Fuc interaction with the donor-binding site predominately through hydrogen bonding between the nucleotide and the base of the donor-binding pocket. The highly flexible Loops 1-3 progressively become ordered while enclosing the sugar nucleotide and locking the donor in place through the Arg^{365}-Asp^{368}-Arg^{441} cage. Binding of the glycan acceptor with its GlcNAc O6 hydroxyl positioned as nucleophile leads to deprotonation by Glu^{373}, in-line S_N2 attack of the donor C1, and shuttling of the proton from Glu^{373} through Lys^{369} to the β-phosphate of the leaving group (Fig. 8*A*). The importance of each of these donor interactions was demonstrated through binding site mutants that all individually led to enzyme inactivation.

Structures of FUT8 acceptor complexes

The structures of several high and low affinity FUT8 acceptor complexes also allowed mapping of steric contributions to substrate binding affinity and specificity. Initial structural studies on the FUT8:GDP:A2-Asn complex identified analogous interactions found in prior structural studies on equivalent complexes (41, 42). The Man-β1,4GlcNAc-β1,4-βAsn acceptor core bound within the cleft between the two Rossmann-folds, whereas the C-terminal SH3 domain presented a flattened surface and steric barrier for branched substrate interactions that established acceptor glycan specificity. Our kinetic analysis of site directed mutants also probed the roles of individual amino acids in substrate binding and catalysis to validate the structural model.

The studies were then extended by examining additional acceptors complexes with reduced binding affinities. The A3'-Asn structure extended the additional β1,4-GlcNAc into solvent relative to the A2-Asn complex (Fig. 7*B*). A similar solvent-exposed β1,4-Gal extension was predicted for the G1 structure based on comparison with the A2-Asn complex. Both acceptor modifications reduce catalytic efficiencies by 3-4–fold likely as a result of entropic penalties from the solvent-exposed sugar rather than steric restrictions.

In contrast, modifications to the ***M3*** residue, especially at the O6 position, led to a steric clash with the enzyme surface (Fig. 7*A*). As a result, both the NM5N2-Asn (α1,6-Man on ***M3***) and A3-Asn (β1,6-GlcNAc on ***M3***) had significant disorder for residues on the ***M3*** branch, whereas the remainder of the acceptor structure was well resolved. This disorder is consistent with reduced catalytic efficiencies for these acceptors (8.4- and 20-fold reduction in k_{cat}/K_m, respectively) and a displacement of the ***M3*** residue as a consequence of the O6 modification. NM5N2-Asn had slightly better catalytic efficiency than A3-Asn, consistent with the well-defined electron density for the ***M3*** residue in the crystal structure and the reduced size of the Man-α1,6- substituent *versus* GlcNAc-β1,6- for A3-Asn. These comparisons of catalytic efficiencies and acceptor complex structures highlight the role of the SH3 domain as a critical binding interface for tuning branch-specific acceptor affinity through both complementarity interactions and steric restrictions.

Conserved and distinctive structural elements for substrate recognition among FUTs

The FUT8 structure also allowed a comparison with other known GT-B fold fucosyltransferases to identify conserved and divergent structural features. These alignments revealed a far more extensive similarity within the core Rossmann-folds and previously noted donor-binding site residues (42) and other regions identified in sequence alignments (95, 101). Surprisingly, no conservation in position or sequence for the three dynamic loops that enclose the FUT8 donor-binding site were identified indicating that the mechanism of induced-fit donor binding was not preserved among the other fucosyltransferases.

Despite the similarities in GT-B fold structure and sugar donor-binding interactions, no structural similarity was observed for the loops involved in acceptor recognition (Fig. S3). POFUT1 and POFUT2 employ deep clefts between the two Rossmann-folds for recognition of their respective protein substrate domains, but use completely different sets of loop interactions (38, 39). AtFUT1 (30) and FUT8 employ a more flattened face of the enzyme surface for acceptor interactions, but also use completely different loop structures and an additional SH3 domain for FUT8.

Catalytic mechanism and evolution of modular substrate recognition by glycosyltransferases

The use of unique acceptor-binding loop insertions in GT-B fold fucosyltransferases is highly reminiscent of hypervariable substrate-binding loops in the evolution of GT-A fold glycosyltransferases (32, 102, 103). In contrast to the two Rossmann domains in GT-B fold enzymes, GT-A fold glycosyltransferases have a single, conserved Rossmann-fold core and employ proximal residues for donor interactions, whereas more divergent extended loop insertions are free to rapidly evolve and diversify novel acceptor specificities (32, 102, 103). This rapid evolution of the loop insertions is constrained by the necessity of positioning the acceptor nucleophile for attack and access to a catalytic base for nucleophile activation relative to the C1 of the

sugar donor. GT-A fold inverting glycosyltransferases have highly conserved positions for the catalytic base, hydroxyl nucleophile, and generally use a conserved *DXD* motif for metal binding and sugar nucleotide positioning (32). For GT-A fold retaining enzymes the position for the hydroxyl nucleophile is shifted to no longer use of the enzyme-associated catalytic base, and instead a donor substrate-assisted S_N1 catalytic mechanism is employed (32).

The present studies on the GT-B fold fucosyltransferases indicate an analogous use of Rossmann-fold core structures, conserved proximal residues for donor interactions, and highly divergent loop regions for distinctive acceptor recognition. Surprisingly, whereas the fucosyltransferases all have inverting catalytic mechanisms, their strategies for use of a catalytic base are quite distinct. AtFUT1 has no discernable catalytic base and water-mediated proton shuttle mechanism has been invoked (30). For POFUT1 the donor β-phosphate oxygen has been proposed as the catalytic base with the possible involvement of a water-mediated proton shuttle (20, 33, 38). FUT8 and POFUT2 (40) both have clearly identified catalytic bases, but they originate from different regions of their protein structures and act from opposite faces in deprotonation of their respective nucleophilic hydroxyls. Thus, despite the highly similar core structures, positions of donor sugars and acceptor nucleophiles among the fucosyltransferases, their respective catalytic base mechanisms are entirely different.

Although a general understanding of GT-A fold glycosyltransferase evolution is emerging (32, 102, 103), a parallel understanding of GT-B fold enzymes has lagged behind largely because of their more complex domain architectures and fewer determined protein structures in complex with substrate analogs. However, evolutionary parallels between the two protein-fold classes are now evident and further insights into selective substrate recognition among the broader collection of GT-B glycosyltransferases will expand our understanding of how diverse glycan structures are elaborated in biological systems.

Experimental procedures

Cloning, expression, fusion tag cleavage, and purification of FUT8 in HEK293F cells

The expression construct encoding the catalytic domain of human FUT8 (α1,6-fucosyltransferase, Uniprot Q9BYC5, residues 41-575) was generated by amplification of a Mammalian Gene Collection clone and transferring it into a pDONR221 vector through Gateway recombination (83). The PCR product, containing the Gateway *att1* recombination sites, was subcloned into a pGEN2-DEST mammalian expression vector that employs a cytomegalovirus promoter and encodes an NH_2-terminal sequence followed by an His_8 tag, an AviTag recognition site, "superfolder" GFP, the 7-amino acid recognition sequence of TEV protease (83), and the coding region of human FUT8. The protein was expressed through transient transfection in either WT HEK293F (Freestyle 293F, ThermoFisher Scientific) cells or mutant HEK293S ($GnTI^-$) cells (ATCC, catalog number CRL-3022). Briefly, cells were maintained in suspension culture at 1-3 $\times$ 10^6 cells/ml in a humidified CO_2 shaker incubator (37 °C, 150 rpm). Transient transfection was performed at a cell density of 3-3.5 $\times$ 10^6 cells/ml in media containing 9 parts of Freestyle™ 293 Expression Medium (Life Technologies) and 1 part of Ex-Cell 293 serum-free medium (Sigma) using polyethyleneimine (linear 25 kDa PEI, Polysciences, Inc., PA) at a concentration of 5 μg/ml and a plasmid DNA concentration of 4 μg/ml. At 24 h post-transfection the suspension cultures were diluted 1:1 with culture media containing valproic acid (2.2 mM final concentration, Sigma). Cultures containing the secreted GFP-tagged protein were harvested 6 days post-transfection. For evaluation of enzyme kinetics, alanine mutants were generated using Q5 site-directed mutagenesis kit (New England Biolabs) and sequences were confirmed for the desired mutations. Both WT and mutant forms were expressed in the pGEN2-DEST vector and expressed as a soluble secreted form.

The WT and mutant forms of the protein were purified as described previously (Table S4) (83, 86). The harvested supernatant was filtered through 0.8-μm filter membrane to remove particulate matter and then loaded onto nickel-nitrilotriacetic acid resin (Qiagen) pre-equilibrated with 20 mM HEPES, pH 7.4, 300 mM NaCl, 20 mM imidazole, and 5% glycerol. After washing steps, the GFP-FUT8 fusion protein was eluted using 300 mM imidazole and further pooled and concentrated for determination of enzyme kinetics. Removal of the GFP tag was performed by treating the concentrated protein with TEV protease at a ratio of 1:5 relative to the fusion protein and incubating the sample for 16 h at 4 °C. The sample was then loaded to a nickel-nitrilotriacetic acid resin to remove the cleaved GFP and His-tagged TEV protease leading to a purified untagged protein in the flow-through fraction. For structural studies, the protein was further purified using a Superdex 75 column (GE Healthcare) pre-equilibrated with 20 mM HEPES, pH 7.4, 150 mM NaCl, and 60 mM imidazole and the peak fractions were collected.

SEC-MALS

The oligomerization of FUT8 was analyzed by injecting the enzyme (20 μl, 1 mg/ml) on an analytical grade Superdex 75 column pre-equilibrated with 25 mM HEPES, pH 7.4, 150 mM NaCl, 0.02% NaN_3. Light scattering and deferential refractive index were measured using a MiniDAWN TREOS detector (Wyatt Tech.) and Optilab rEx detector (Wyatt Tech.) respectively. Data were analyzed using the ASTRA 6.0 software (Wyatt Tech.)

Alkaline phosphatase treatment of GDP-fucose

For enzyme kinetics, GDP-fucose (Carbosynth) was used as donor at a final concentration of 0.2 mM. Prior to performing the assay, GDP-fucose was treated with calf intestinal alkaline phosphatase (CIAP, Promega) to remove free GDP. Briefly, a reaction mix of 3 units/µl of CIAP/50 µl of 50 mM GDP-fucose in 1× CIAP buffer (5 µl) was prepared in a microcentrifuge tube. Multiple doses of CIAP (3 units/µl) were added every 2 h and incubated for a total of 6 h at 37 °C with gentle shaking (~100-150 rpm). After 6 h, the concentration of GDP-fucose in the reaction volume was adjusted to 20 mM. The entire reaction mix was filtered through a Microcon 10-kDa centrifugal filter

unit (Millipore) with Ultracel-10 membrane by centrifuging at 14,000 × *g* for 30 min to remove CIAP. The filtrate was recovered and incubated with another 3 units of CIAP for 16 h at 37 °C with gentle shaking (~100-150 rpm). Finally, the reaction mix was further filtered through a Microcon 10-kDa centrifugal filter unit as mentioned above. The filtrate was stored at −20 °C and used as the stock solution of GDP-fucose. The CIAP-treated GDP-fucose gave lower background and improved signal to noise ratio in enzyme kinetic assays compared with untreated GDP-fucose.

FUT8 kinetic analysis

Enzyme kinetics for the WT and mutant form of the enzyme were determined using the GDP-Glo™ Glycosyltransferase assay (Promega) that detects GDP as a released product of the glycosyltransferase reaction. Assays were performed in a 10-μl reaction volume consisting of a universal buffer (200 mM each of Tris, MES, MOPS, pH 7.5), 0.2 mM GDP-fucose (CIAP-treated, see above) in reactions containing varied concentrations of the respective glycan substrates: A1-Asn, A2-Asn, A3-Asn, A3'-Asn, A4-Asn, G1-Asn, NM5N2-Asn, M3N2-Asn, and M5N2-Asn-Fmoc. Reactions were carried out using purified GFP-fusion enzyme (WT or alanine mutants) at 37 °C for 30 min. For acceptor titration, assays were performed using the desired substrate at a concentration range of 0-1 mM with 0.2 mM GDP-fucose as final concentration of donor. Similarly, for donor titration, reactions were carried out using GDP-fucose (0-0.2 mM) with 0.5-1 mM A2-Asn as final concentration. Reactions were stopped using 5 μl of GDP-detection reagent at a 1:1 ratio in a white, opaque 384-well–plate and incubated in dark for 1 h at room temperature. The released GDP product was detected based on luminescence using a GloMax Multidetection plate reader (Promega). The steady state parameters of K_m, k_{cat}, and V_{max} values were calculated using a GDP standard curve and nonlinear curve fitting in GraphPad Prism 6 software.

Synthesis of oligosaccharide acceptors

The glycan acceptors (A1-Asn, G1-Asn, A2-Asn, A3-Asn, A3'-Asn, and A4-Asn) were synthesized employing established chemoenzymatic methods for *N*-glycan synthesis (104, 105). The human MGAT1, MGAT4, and MGAT5 glycosyltransferases used in the synthesis were expressed in the HEK293 cell expression system as previously described (83). Briefly, a sialylglycopeptide ($Neu5Ac_2Gal_2GlcNAc_2Man_3GlcNAc_2$-peptide) isolated from hen egg yolk powder (106) was treated with *Clostridium perfringens* neuraminidase (New England Biolabs) to produce the G2-peptide, and further treated with *Aspergillus niger β-gal* (Megazyme) to generate the A2-peptide. The glycopeptide was then exhaustively treated with Pronase from *Streptomyces griseus* (Sigma-Aldrich) to trim the peptide to a single Asn residue and generate A2-Asn ($GlcNAc_2Man_3GlcNAc_2$-Asn). Treatment of A2-Asn with human MGAT4 or MGAT5 in the presence of UDP-GlcNAc produced the two acceptors, A3'-Asn and A3-Asn, respectively, with the composition of $GlcNAc_3Man_3GlcNAc_2$-Asn. Treating the A2-Asn with both MGAT4 and MGAT5 provided acceptor A4-Asn ($GlcNAc_4Man_3GlcNAc_2$-Asn).

Treatment of A2-Asn with *Streptococcus pneumoniae N*-acetylglucosaminidase (New England Biolabs) generated Man3-Asn, which was then treated with MGAT1 in the presence of UDP-GlcNAc to generate A1-Asn ($GlcNAcMan_3GlcNAc_2$-Asn). G1-Asn ($GalGlcNAc_2Man_3GlcNAc_2$-Asn) was obtained by treating G2-peptide with *Escherichia coli β-gal* (Sigma-Aldrich), which preferentially cleaves the galactose on the MGAT1 branch (105, 107), followed by Pronase treatment.

NM5N2-Asn ($GlcNAcMan_5GlcNAc_2$-Asn) and Man5N2-Asn-Fmoc ($Man_5GlcNAc_2$-Asn-Fmoc) were prepared from $Man_9GlcNAc_2$-Asn isolated from soybean agglutinin (108). The crude soybean agglutinin isolated from soybean flour was digested with Pronase (Sigma Aldrich) and purified to afford $Man_9GlcNAc_2$-Asn, which was subsequently treated with *Bacteriodes thetaiotaomicron* α1,2-mannosidase to provide Man5N2-Asn. Installation of the Fmoc group produced Man5N2-Asn-Fmoc, which was subsequently treated with human MGAT1 in the presence of UDP-GlcNAc, followed by Fmoc removal to provide NMan5N2-Asn ($GlcNAcMan_5GlcNAc_2$-Asn).

Crystallization and data collection

The catalytic domain of FUT8 (10 mg/ml in a storage buffer containing 20 mM HEPES, pH 7.5, 50 mM NaCl, 300 mM betaine) was mixed with GDP or with GDP plus acceptor and screened for crystallization conditions using a TTP Labtech Mosquito Crystal robot and optimized using hanging drop vapor diffusion with 2-μl drops (1:1 protein:reservoir ratio). For the FUT8:GDP complex, crystals containing 5 mM GDP grew in less than 1 week from a reservoir of 1.4 M ammonium sulfate, 0.6 M L-proline, 0.1 M HEPES, pH 7.5. Crystals were transferred to the reservoir solution supplemented with 5 mM GDP, and 20% cryoprotectant (1:1:1 ethylene glycol, DMSO, and glycerol). FUT8:GDP crystallized in space group $P6_5$ and diffracted to 2.25 Å (Table S2).

For the FUT8:GDP:A2-Asn complex, 10 mg/ml of protein was prepared in storage buffer containing 5 mM GDP and 5 mM A2-Asn and crystals grew from a reservoir solution of 1 M lithium sulfate, 10 mM nickel chloride, and 0.1 M Tris, pH 8.5. Crystals were transferred to the reservoir solution supplemented with 5 mM GDP, 5 mM A2-Asn, and 20% cryoprotectant (1:1:1 ethylene glycol, DMSO, and glycerol). FUT8:GDP:A2-Asn crystallized in space group $P6_522$ and diffracted to 2.4 Å (Table S2).

For the FUT8:GDP:A3'-Asn complex, 10 mg/ml of protein was prepared in storage buffer containing 10 mM GDP and 10 mM A3'-Asn and crystals grew from a reservoir solution of 1.2 M lithium sulfate, 12 mM nickel chloride, and 0.1 M Tris, pH 8.5. Crystals were transferred to the reservoir solution supplemented with 10 mM GDP, 10 mM A3'-Asn. A 40:60 mixture of paratone and paraffin was used as the cryoprotectant. FUT8:GDP:A3'-Asn crystallized in space group $P6_522$ and diffracted to 3.3 Å (Table S2).

For the FUT8:GDP:A3-Asn complex, 10 mg/ml of protein was prepared in storage buffer containing 10 mM GDP and 10 mM A3-Asn and crystals grew overnight from a reservoir solution of 0.2 M L-proline, 10% PEG3350, and 0.1 M HEPES, pH 7.2.

Crystals were transferred to the reservoir solution supplemented with 10 mM GDP, 10 mM A3'-Asn, and 18% cryoprotectant (1:1:1 ethylene glycol, DMSO, and glycerol) supplemented with 0.2 M sodium ascorbate. FUT8:GDP:A3-Asn crystallized in space group $P6_5$ and diffracted to 2.47 Å (Table S2).

For the FUT8:GDP:NM5M2-Asn complex, 10 mg/ml of protein in storage buffer containing 10 mM GDP and 10 mM NM5M2-Asn was prepared and crystals grew from a reservoir solution of 0.2 M ammonium chloride, 10% PEG3350. Crystals were transferred to the reservoir solution supplemented with 10 mM GDP, 10 mM NM5M2-Asn, and 18% cryoprotectant (1:1:1 ethylene glycol, DMSO, and glycerol). FUT8:GDP:NM5N2-Asn crystallized in space group $P6_5$ and diffracted to 3.2 Å (Table S2).

All cryo-protected crystals were flash cooled in liquid nitrogen and X-ray data were collected at the SER-CAT 22-BM beamline using a MAR-CCD detector (FUT8:GDP and FUT8:GDP:A2-Asn) or at the 22-ID beamline using an Eiger-16M detector (FUT8:GDP:A3-Asn, FUT8:GDP:A3'-Asn, and FUT8:GDP:NM5N2-Asn) at the Argonne National Laboratory. The data were processed using XDS (109). Five percent of the data were set aside for cross-validation.

Phasing and refinement

The crystal structures of FUT8:GDP and FUT8:GDP:A2-Asn were solved using molecular replacement with the apo-FUT8 structure (PDB 2DE0 (36)) as the search model. The NH_2-terminus (residues 41-107) and the C-terminal residue Lys^{575} were disordered and left unmodeled. Successive rounds of automated refinement in Phenix (110) and iterative manual fitting using Coot (111) produced the final models (Table S2). The B-factors were refined using TLS (112).

The crystal structures of FUT8:GDP:A3'-Asn, FUT8:GDP:A3-Asn, and FUT8:NM5N2-Asn were solved using molecular replacement with FUT8:A2-Asn as the search model. In FUT8:GDP:A3'-Asn, the NH_2 terminus (residues 41-107) and C terminus (residues 574-575) were disordered and left unmodeled. Similarly, in FUT8:GDP:A3-Asn, the NH_2 terminus (residues 41-107 in chains A, B, C, D, and F, and 41-108 in chains E, G, and H) and C terminus (residue 575 in all chains) were left unmodeled. In FUT8:NM5N2-Asn, the NH_2 terminus (residues 41-107) and C terminus (residue 575) were not modeled. All three structural models were refined like FUT8:GDP and their respective statistics are reported in Table S2. Data intensity statistics from Xtriage (110) for FUT8:GDP:A3-Asn and FUT8:GDP:NM5N2-Asn indicated the presence of merohedral twinning with the twin operator (h, -h-k, -l). The twin fraction k_i refined to 0.25 for FUT8:GDP:A3-Asn and to 0.15 for the FUT8:GDP:NM5N2-Asn datasets, respectively.

During structural refinement, geometrical restraints were used to restrain monosaccharides with weak electron density in the lowest energy chair conformation ($^4C_1$) (110, 113). The linkage torsion angles for the glycosidic bonds (ϕ, ψ) in FUT8:A2-Asn, FUT8:A3'-Asn, FUT8:A3-Asn, and FUT8:NM5N2-Asn complexes were determined using the Carbohydrate Ramachandran Plot (*CaRP*) and fall into the energetically preferred areas of the GlyTorsion plot (114).

FUT8 loop residues Pro^{299}, Pro^{305}, and Pro^{358} form cis-peptide bonds, none of which are conserved in the NodZ:GDP complex (PDB code 3SIX (35)), the human POFUT2:GDP:Fuc complex (PDB 4AP6 (40)), the *C. elegans* POFUT2:GDP:thrombospondin repeat complex (PDB 5FOE (39)) or the AtFUT1:GDP:xylo-oligosaccahride complex (PDB 5KOR (29)). However, the mouse POFUT1:GDP-Fuc:EGF domain complex (PDB 5KY3 (38)) conserves one of the cis-peptide bonds (H357:P358) as R237:P238 in the sequence.

Structural analysis

Structure based sequence alignment was performed using default parameters on the PROMALS3D server (97) using structures of the human FUT8:GDP:A2-Asn complex, mouse POFUT1:GDP-Fuc:EGF domain complex (PDB 5KY3 (38)), the *C. elegans* POFUT2:GDP:thrombospondin repeat complex (PDB 5FOE (39)), the human POFUT2:GDP-Fuc complex (PDB 4AP6 (40)), the NodZ:GDP complex (PDB 3SIX (35)), and the AtFUT1:GDP:xylo-oligosaccahride complex (PDB 5KOR (29)). Alignment of the structural models was performed in Coot (111) followed by manual adjustment in PyMOL and displayed using PyMOL (Schrödinger). Structural elements identified in the PROMALS3D analysis were extracted from the full protein alignment for display as an overlay of the respective structures. The difference density maps ($F_o - F_c$) shown in the figures for the bound GDP and the A2 acceptor were calculated subsequent to structure solution and initial restrained refinement of the polypeptide, but prior to the modeling of the respective ligands. In all cases, the final refined coordinates were used to depict the ligand model. Polder maps (115) for the A3'-Asn, A3-Asn, and NM5N2-Asn acceptors were calculated following a modified procedure to reduce model bias (103). Briefly, prior to calculating the Polder map, the acceptor was omitted and the remaining model subjected to Cartesian simulated annealing at 5000 K. The acceptor coordinates were then used to calculate a reduced-bias Polder map.

Data availability

All atomic coordinates and structure factors were deposited in the RCSB Protein Data Bank (PDB) under accession codes 6X5H (FUT8:GDP), 6X5R (FUT8:GDP:A2), 6X5T (FUT8:GDP:A3), 6X5S (FUT8:GDP:A3') and 6X5U (FUT8:GDP:NM5N2).

Acknowledgments—We are grateful for the technical support of Rosemary Kim.

Author contributions—B. M. B., R. K., Z. A. W., and K. W. M. conceptualization; B. M. B., R. K., L. L., A. R., C. L., G. Z., G. P. B., J-Y. Y., L-X. W., G-J. B., Z. A. W., and K. W. M. resources; B. M. B., R. K., Z. A. W., and K. W. M. data curation; B. M. B., R. K., Z. A. W., and K. W. M. formal analysis; B. M. B., R. K., L-X. W., G-J. B., Z. A. W., and K. W. M. validation; B. M. B., R. K., Z. A. W., and K. W. M. investigation; B. M. B., R. K., L. L., A. R., C. L., G. Z., G. P. B., J-Y. Y., L-X. W., G-J. B., Z. A. W., and K. W. M. methodology; B. M. B., R. K., Z. A. W., and K. W. M. writing-original draft; B. M. B., R. K., Z. A. W., and K. W. M. writing-review and editing;

L-X. W., G-J. B., Z. A. W., and K. W. M. supervision; Z. A. W. and K. W. M. funding acquisition; Z. A. W. and K. W. M. project administration; K. W. M. visualization.

Funding and additional information—This work was supported by National Institutes of Health Grants R01GM130915 (to K. W. M., and Z. A. W.), P41GM103390 (to K. W. M., and G. J. B.), P01GM107012 (to K. W. M., and G. J. B.), and R01GM080374 (to L-X. W.). The content is solely the responsibility of the authors and does not necessarily represent the official views of the National Institutes of Health.

Conflict of interest—The authors declare that they have no conflicts of interest with the contents of this article.

Abbreviations—The abbreviations used are: EGF, epidermal growth factor; SEC-MALS, size exclusion-multiangle light scattering; POFUT, protein-O-fucosyltransferase; rmsd, root mean square deviation; SH3, Src homology 3; CIAP, calf intestinal alkaline phosphatase; TEV, tobacco etch virus; Fmoc, N-(9-fluorenyl)methoxycarbonyl.

References

1. Barb, A. W., Meng, L., Gao, Z., Johnson, R. W., Moremen, K. W., and Prestegard, J. H. (2012) NMR characterization of immunoglobulin G Fc glycan motion on enzymatic sialylation. *Biochemistry* **51,** 4618–4626 CrossRef Medline
2. Varki, A. (1993) Biological roles of oligosaccharides: all of the theories are correct. *Glycobiology* **3,** 97–130 CrossRef Medline
3. Varki, A. (2017) Biological roles of glycans. *Glycobiology* **27,** 3–49 CrossRef Medline
4. Cummings, R. D., and Pierce, J. M. (2014) The challenge and promise of glycomics. *Chem. Biol.* **21,** 1–15 CrossRef Medline
5. Li, W., Yu, R., Ma, B., Yang, Y., Jiao, X., Liu, Y., Cao, H., Dong, W., Liu, L., Ma, K., Fukuda, T., Liu, Q., Ma, T., Wang, Z., Gu, J., *et al.* (2015) Core fucosylation of IgG B cell receptor is required for antigen recognition and antibody production. *J. Immunol.* **194,** 2596–2606 CrossRef Medline
6. Shields, R. L., Lai, J., Keck, R., O'Connell, L. Y., Hong, K., Meng, Y. G., Weikert, S. H., and Presta, L. G. (2002) Lack of fucose on human IgG1 *N*-linked oligosaccharide improves binding to human Fcγ RIII and antibody-dependent cellular toxicity. *J. Biol. Chem.* **277,** 26733–26740 CrossRef Medline
7. Subedi, G. P., Falconer, D. J., and Barb, A. W. (2017) Carbohydrate-polypeptide contacts in the antibody receptor CD16A identified through solution NMR spectroscopy. *Biochemistry* **56,** 3174–3177 CrossRef Medline
8. Iijima, J., Kobayashi, S., Kitazume, S., Kizuka, Y., Fujinawa, R., Korekane, H., Shibata, T., Saitoh, S. I., Akashi-Takamura, S., Miyake, K., Miyoshi, E., and Taniguchi, N. (2017) Core fucose is critical for CD14-dependent Toll-like receptor 4 signaling. *Glycobiology* **27,** 1006–1015 CrossRef Medline
9. Li, W., Ishihara, K., Yokota, T., Nakagawa, T., Koyama, N., Jin, J., Mizuno-Horikawa, Y., Wang, X., Miyoshi, E., Taniguchi, N., and Kondo, A. (2008) Reduced alpha4beta1 integrin/VCAM-1 interactions lead to impaired pre-B cell repopulation in alpha1,6-fucosyltransferase deficient mice. *Glycobiology* **18,** 114–124 CrossRef Medline
10. Liang, W., Mao, S., Sun, S., Li, M., Li, Z., Yu, R., Ma, T., Gu, J., Zhang, J., Taniguchi, N., and Li, W. (2018) Core fucosylation of the T cell receptor is required for T cell activation. *Front. Immunol.* **9,** 78 CrossRef Medline
11. Matsumoto, K., Yokote, H., Arao, T., Maegawa, M., Tanaka, K., Fujita, Y., Shimizu, C., Hanafusa, T., Fujiwara, Y., and Nishio, K. (2008) N-Glycan fucosylation of epidermal growth factor receptor modulates receptor activity and sensitivity to epidermal growth factor receptor tyrosine kinase inhibitor. *Cancer Sci.* **99,** 1611–1617 CrossRef Medline
12. Nakayama, K., Wakamatsu, K., Fujii, H., Shinzaki, S., Takamatsu, S., Kitazume, S., Kamada, Y., Takehara, T., Taniguchi, N., and Miyoshi, E. (2019) Core fucose is essential glycosylation for CD14-dependent Toll-like receptor 4 and Toll-like receptor 2 signalling in macrophages. *J. Biochem.* **165,** 227–237 CrossRef Medline
13. Pinho, S. S., Seruca, R., Gärtner, F., Yamaguchi, Y., Gu, J., Taniguchi, N., and Reis, C. A. (2011) Modulation of E-cadherin function and dysfunction by *N*-glycosylation. *Cell Mol. Life Sci.* **68,** 1011–1020 CrossRef Medline
14. Wang, X., Gu, J., Ihara, H., Miyoshi, E., Honke, K., and Taniguchi, N. (2006) Core fucosylation regulates epidermal growth factor receptor-mediated intracellular signaling. *J. Biol. Chem.* **281,** 2572–2577 CrossRef Medline
15. Zhao, Y., Itoh, S., Wang, X., Isaji, T., Miyoshi, E., Kariya, Y., Miyazaki, K., Kawasaki, N., Taniguchi, N., and Gu, J. (2006) Deletion of core fucosylation on alpha3beta1 integrin down-regulates its functions. *J. Biol. Chem.* **281,** 38343–38350 CrossRef Medline
16. Manabe, Y., Marchetti, R., Takakura, Y., Nagasaki, M., Nihei, W., Takebe, T., Tanaka, K., Kabayama, K., Chiodo, F., Hanashima, S., Kamada, Y., Miyoshi, E., Dulal, H. P., Yamaguchi, Y., Adachi, Y., *et al.* (2019) The core fucose on an IgG antibody is an endogenous ligand of Dectin-1. *Angew. Chem. Int. Ed. Engl.* **58,** 18697–18702 CrossRef Medline
17. Falconer, D. J., Subedi, G. P., Marcella, A. M., and Barb, A. W. (2018) Antibody fucosylation lowers the FcγRIIIa/CD16a affinity by limiting the conformations sampled by the N162-glycan. *ACS Chem. Biol.* **13,** 2179–2189 CrossRef Medline
18. Schneider, M., Al-Shareffi, E., and Haltiwanger, R. S. (2017) Biological functions of fucose in mammals. *Glycobiology* **27,** 601–618 CrossRef Medline
19. Lombard, V., Golaconda Ramulu, H., Drula, E., Coutinho, P. M., and Henrissat, B. (2014) The carbohydrate-active enzymes database (CAZy) in 2013. *Nucleic Acids Res.* **42,** D490–D495 CrossRef Medline
20. Lira-Navarrete, E., and Hurtado-Guerrero, R. (2018) A perspective on structural and mechanistic aspects of protein O-fucosylation. *Acta Crystallogr. F Struct. Biol. Commun.* **74,** 443–450 CrossRef Medline
21. Scharberg, E. A., Olsen, C., and Bugert, P. (2016) The H blood group system. *Immunohematology* **32,** 112–118 Medline
22. Stowell, C. P., and Stowell, S. R. (2019) Biologic roles of the ABH and Lewis histo-blood group antigens part I: infection and immunity. *Vox Sang.* **114,** 426–442 CrossRef Medline
23. Lowe, J. B. (1993) The blood group-specific human glycosyltransferases. *Baillieres Clin. Haematol.* **6,** 465–492 CrossRef Medline
24. Costache, M., Cailleau, A., Fernandez-Mateos, P., Oriol, R., and Mollicone, R. (1997) Advances in molecular genetics of alpha-2- and alpha-3/4-fucosyltransferases. *Transfus. Clin. Biol.* **4,** 367–382 CrossRef Medline
25. Ma, B., Simala-Grant, J. L., and Taylor, D. E. (2006) Fucosylation in prokaryotes and eukaryotes. *Glycobiology* **16,** 158R–184R CrossRef Medline
26. Ihara, H., Tsukamoto, H., Gu, J., Miyoshi, E., Taniguchi, N., and Ikeda, Y. (2014) Fucosyltransferase 8: GDP-fucose N-glycan core α6-fucosyltransferase (FUT8). in *Handbook of Glycosyltransferases and Related Genes* (Taniguchi, N., Honke, K., Fukuda, M., Narimatsu, H., Yamaguchi, Y., and Angata, T., eds) 2nd Ed., pp. 581–596, Springer, Tokyo, Japan
27. Kizuka, Y., and Taniguchi, N. (2016) Enzymes for N-glycan branching and their genetic and nongenetic regulation in cancer. *Biomolecules* **6,** 25 CrossRef
28. Nagae, M., Yamaguchi, Y., Taniguchi, N., and Kizuka, Y. (2020) 3D structure and function of glycosyltransferases involved in N-glycan maturation. *Int. J. Mol. Sci.* **21,** 437 CrossRef
29. Rocha, J., Ciceron, F., de Sanctis, D., Lelimousin, M., Chazalet, V., Lerouxel, O., and Breton, C. (2016) Structure of *Arabidopsis thaliana* FUT1 reveals a variant of the GT-B class fold and provides insight into Xyloglucan fucosylation. *Plant Cell* **28,** 2352–2364 CrossRef Medline
30. Urbanowicz, B. R., Bharadwaj, V. S., Alahuhta, M., Peña, M. J., Lunin, V. V., Bomble, Y. J., Wang, S., Yang, J. Y., Tuomivaara, S. T., Himmel, M. E., Moremen, K. W., York, W. S., and Crowley, M. F. (2017) Structural, mutagenic and *in silico* studies of xyloglucan fucosylation in *Arabidopsis thaliana* suggest a water-mediated mechanism. *Plant J.* **91,** 931–949 CrossRef Medline

31. Van Der Wel, H., Fisher, S. Z., and West, C. M. (2002) A bifunctional diglycosyltransferase forms the Fucα1,2Galβ1,3-disaccharide on Skp1 in the cytoplasm of dictyostelium. *J. Biol. Chem.* **277,** 46527–46534 CrossRef Medline
32. Moremen, K. W., and Haltiwanger, R. S. (2019) Emerging structural insights into glycosyltransferase-mediated synthesis of glycans. *Nat. Chem. Biol.* **15,** 853–864 CrossRef Medline
33. Lira-Navarrete, E., Valero-González, J., Villanueva, R., Martínez-Júlvez, M., Tejero, T., Merino, P., Panjikar, S., and Hurtado-Guerrero, R. (2011) Structural insights into the mechanism of protein O-fucosylation. *PLoS ONE* **6,** e25365 CrossRef Medline
34. Sun, H. Y., Lin, S. W., Ko, T. P., Pan, J. F., Liu, C. L., Lin, C. N., Wang, A. H., and Lin, C. H. (2007) Structure and mechanism of *Helicobacter pylori* fucosyltransferase: a basis for lipopolysaccharide variation and inhibitor design. *J. Biol. Chem.* **282,** 9973–9982 CrossRef Medline
35. Brzezinski, K., Dauter, Z., and Jaskolski, M. (2012) Structures of NodZ α1,6-fucosyltransferase in complex with GDP and GDP-fucose. *Acta Crystallogr. D Biol. Crystallogr.* **68,** 160–168 CrossRef Medline
36. Ihara, H., Ikeda, Y., Toma, S., Wang, X., Suzuki, T., Gu, J., Miyoshi, E., Tsukihara, T., Honke, K., Matsumoto, A., Nakagawa, A., and Taniguchi, N. (2007) Crystal structure of mammalian alpha1,6-fucosyltransferase, FUT8. *Glycobiology* **17,** 455–466 CrossRef Medline
37. McMillan, B. J., Zimmerman, B., Egan, E. D., Lofgren, M., Xu, X., Hesser, A., and Blacklow, S. C. (2017) Structure of human POFUT1, its requirement in ligand-independent oncogenic Notch signaling, and functional effects of Dowling-Degos mutations. *Glycobiology* **27,** 777–786 CrossRef Medline
38. Li, Z., Han, K., Pak, J. E., Satkunarajah, M., Zhou, D., and Rini, J. M. (2017) Recognition of EGF-like domains by the Notch-modifying O-fucosyltransferase POFUT1. *Nat. Chem. Biol.* **13,** 757–763 CrossRef Medline
39. Valero-Gonzalez, J., Leonhard-Melief, C., Lira-Navarrete, E., Jimenez-Oses, G., Hernandez-Ruiz, C., Pallares, M. C., Yruela, I., Vasudevan, D., Lostao, A., Corzana, F., Takeuchi, H., Haltiwanger, R. S., and Hurtado-Guerrero, R. (2016) A proactive role of water molecules in acceptor recognition by protein *O*-fucosyltransferase 2. *Nat. Chem. Biol.* **12,** 240–246 CrossRef Medline
40. Chen, C. I., Keusch, J. J., Klein, D., Hess, D., Hofsteenge, J., and Gut, H. (2012) Structure of human POFUT2: insights into thrombospondin type 1 repeat fold and O-fucosylation. *EMBO J.* **31,** 3183–3197 CrossRef Medline
41. García-García, A., Ceballos-Laita, L., Serna, S., Artschwager, R., Reichardt, N. C., Corzana, F., and Hurtado-Guerrero, R. (2020) Structural basis for substrate specificity and catalysis of alpha1,6-fucosyltransferase. *Nat. Commun.* **11,** 973 CrossRef Medline
42. Järva, M. A., Dramicanin, M., Lingford, J. P., Mao, R., John, A., Jarman, K. E., Grinter, R., and Goddard-Borger, E. D. (2020) Structural basis of substrate recognition and catalysis by fucosyltransferase 8. *J. Biol. Chem.* **295,** 6677–6688 CrossRef
43. Lairson, L. L., Henrissat, B., Davies, G. J., and Withers, S. G. (2008) Glycosyltransferases: structures, functions, and mechanisms. *Annu. Rev. Biochem.* **77,** 521–555 CrossRef Medline
44. Wang, X., Inoue, S., Gu, J., Miyoshi, E., Noda, K., Li, W., Mizuno-Horikawa, Y., Nakano, M., Asahi, M., Takahashi, M., Uozumi, N., Ihara, S., Lee, S. H., Ikeda, Y., Yamaguchi, Y., *et al.* (2005) Dysregulation of TGF-β1 receptor activation leads to abnormal lung development and emphysema-like phenotype in core fucose-deficient mice. *Proc. Natl. Acad. Sci. U.S.A.* **102,** 15791–15796 CrossRef Medline
45. Wang, X., Gu, J., Miyoshi, E., Honke, K., and Taniguchi, N. (2006) Phenotype changes of Fut8 knockout mouse: core fucosylation is crucial for the function of growth factor receptor(s). *Methods Enzymol.* **417,** 11–22 CrossRef Medline
46. Fujii, H., Shinzaki, S., Iijima, H., Wakamatsu, K., Iwamoto, C., Sobajima, T., Kuwahara, R., Hiyama, S., Hayashi, Y., Takamatsu, S., Uozumi, N., Kamada, Y., Tsujii, M., Taniguchi, N., Takehara, T., *et al.* (2016) Core fucosylation on T cells, required for activation of T-cell receptor signaling and induction of colitis in mice, is increased in patients with inflammatory bowel disease. *Gastroenterology* **150,** 1620–1632 CrossRef Medline
47. Gu, W., Fukuda, T., Isaji, T., Hang, Q., Lee, H. H., Sakai, S., Morise, J., Mitoma, J., Higashi, H., Taniguchi, N., Yawo, H., Oka, S., and Gu, J. (2015) Loss of α1,6-fucosyltransferase decreases hippocampal long term potentiation: implications for core fucosylation in the regulation of AMPA receptor heteromerization and cellular signaling. *J. Biol. Chem.* **290,** 17566–17575 CrossRef Medline
48. Fukuda, T., Hashimoto, H., Okayasu, N., Kameyama, A., Onogi, H., Nakagawasai, O., Nakazawa, T., Kurosawa, T., Hao, Y., Isaji, T., Tadano, T., Narimatsu, H., Taniguchi, N., and Gu, J. (2011) α1,6-Fucosyltransferase-deficient mice exhibit multiple behavioral abnormalities associated with a schizophrenia-like phenotype: importance of the balance between the dopamine and serotonin systems. *J. Biol. Chem.* **286,** 18434–18443 CrossRef Medline
49. Lu, X., Zhang, D., Shoji, H., Duan, C., Zhang, G., Isaji, T., Wang, Y., Fukuda, T., and Gu, J. (2019) Deficiency of α1,6-fucosyltransferase promotes neuroinflammation by increasing the sensitivity of glial cells to inflammatory mediators. *Biochim. Biophys. Acta* **1863,** 598–608 CrossRef Medline
50. Ng, B. G., Dastsooz, H., Silawi, M., Habibzadeh, P., Jahan, S. B., Fard, M. A. F., Halliday, B. J., Raymond, K., Ruzhnikov, M. R. Z., Tabatabaei, Z., Taghipour-Sheshdeh, A., Brimble, E., Robertson, S. P., Faghihi, M. A., and Freeze, H. H. (2020) Expanding the molecular and clinical phenotypes of FUT8-CDG. *J. Inherit. Metab. Dis.* **43,** 871–879 CrossRef Medline
51. Ng, B. G., Xu, G., Chandy, N., Steyermark, J., Shinde, D. N., Radtke, K., Raymond, K., Lebrilla, C. B., AlAsmari, A., Suchy, S. F., Powis, Z., Faqeih, E. A., Berry, S. A., Kronn, D. F., and Freeze, H. H. (2018) Biallelic mutations in FUT8 cause a congenital disorder of glycosylation with defective fucosylation. *Am. J. Hum. Genet.* **102,** 188–195 CrossRef Medline
52. Chen, C. Y., Jan, Y. H., Juan, Y. H., Yang, C. J., Huang, M. S., Yu, C. J., Yang, P. C., Hsiao, M., Hsu, T. L., and Wong, C. H. (2013) Fucosyltransferase 8 as a functional regulator of nonsmall cell lung cancer. *Proc. Natl. Acad. Sci. U.S.A.* **110,** 630–635 CrossRef Medline
53. Höti, N., Yang, S., Hu, Y., Shah, P., Haffner, M. C., and Zhang, H. (2018) Overexpression of α(1,6)-fucosyltransferase in the development of castration-resistant prostate cancer cells. *Prostate Cancer Prostatic Dis.* **21,** 137–146 CrossRef Medline
54. Hutchinson, W. L., Du, M. Q., Johnson, P. J., and Williams, R. (1991) Fucosyltransferases: differential plasma and tissue alterations in hepatocellular carcinoma and cirrhosis. *Hepatology* **13,** 683–688 CrossRef Medline
55. Ito, Y., Miyauchi, A., Yoshida, H., Uruno, T., Nakano, K., Takamura, Y., Miya, A., Kobayashi, K., Yokozawa, T., Matsuzuka, F., Taniguchi, N., Matsuura, N., Kuma, K., and Miyoshi, E. (2003) Expression of α1,6-fucosyltransferase (FUT8) in papillary carcinoma of the thyroid: its linkage to biological aggressiveness and anaplastic transformation. *Cancer Lett.* **200,** 167–172 CrossRef Medline
56. Liu, Y. C., Yen, H. Y., Chen, C. Y., Chen, C. H., Cheng, P. F., Juan, Y. H., Chen, C. H., Khoo, K. H., Yu, C. J., Yang, P. C., Hsu, T. L., and Wong, C. H. (2011) Sialylation and fucosylation of epidermal growth factor receptor suppress its dimerization and activation in lung cancer cells. *Proc. Natl. Acad. Sci. U.S.A.* **108,** 11332–11337 CrossRef Medline
57. Muinelo-Romay, L., Vazquez-Martín, C., Villar-Portela, S., Cuevas, E., Gil-Martín, E., and Fernández-Briera, A. (2008) Expression and enzyme activity of α(1,6)fucosyltransferase in human colorectal cancer. *Int. J. Cancer* **123,** 641–646 CrossRef Medline
58. Shao, K., Chen, Z. Y., Gautam, S., Deng, N. H., Zhou, Y., and Wu, X. Z. (2016) Posttranslational modification of E-cadherin by core fucosylation regulates Src activation and induces epithelial-mesenchymal transition-like process in lung cancer cells. *Glycobiology* **26,** 142–154 CrossRef Medline
59. Tada, K., Ohta, M., Hidano, S., Watanabe, K., Hirashita, T., Oshima, Y., Fujnaga, A., Nakanuma, H., Masuda, T., Endo, Y., Takeuchi, Y., Iwashita, Y., Kobayashi, T., and Inomata, M. (2020) Fucosyltransferase 8 plays a crucial role in the invasion and metastasis of pancreatic ductal adenocarcinoma. *Surg. Today* **50,** 767–777 CrossRef
60. Takahashi, T., Ikeda, Y., Miyoshi, E., Yaginuma, Y., Ishikawa, M., and Taniguchi, N. (2000) α1,6-Fucosyltransferase is highly and specifically

expressed in human ovarian serous adenocarcinomas. *Int. J. Cancer* **88,** 914–919 CrossRef

61. Tu, C. F., Wu, M. Y., Lin, Y. C., Kannagi, R., and Yang, R. B. (2017) FUT8 promotes breast cancer cell invasiveness by remodeling TGF-β receptor core fucosylation. *Breast Cancer Res.* **19,** 111 CrossRef Medline
62. Wang, X., Chen, J., Li, Q. K., Peskoe, S. B., Zhang, B., Choi, C., Platz, E. A., and Zhang, H. (2014) Overexpression of α(1,6)-fucosyltransferase associated with aggressive prostate cancer. *Glycobiology* **24,** 935–944 CrossRef Medline
63. Wang, Y., Fukuda, T., Isaji, T., Lu, J., Im, S., Hang, Q., Gu, W., Hou, S., Ohtsubo, K., and Gu, J. (2015) Loss of α1,6-fucosyltransferase inhibits chemical-induced hepatocellular carcinoma and tumorigenesis by down-regulating several cell signaling pathways. *FASEB J.* **29,** 3217–3227 CrossRef Medline
64. Aoyagi, Y., Isokawa, O., Suda, T., Watanabe, M., Suzuki, Y., and Asakura, H. (1998) The fucosylation index of α-fetoprotein as a possible prognostic indicator for patients with hepatocellular carcinoma. *Cancer* **83,** 2076–2082 CrossRef Medline
65. Flores, A., and Marrero, J. A. (2014) Emerging trends in hepatocellular carcinoma: focus on diagnosis and therapeutics. *Clin. Med. Insights Oncol.* **8,** 71–76 CrossRef Medline
66. Saldova, R., Fan, Y., Fitzpatrick, J. M., Watson, R. W., and Rudd, P. M. (2011) Core fucosylation and α-3 sialylation in serum *N*-glycome is significantly increased in prostate cancer comparing to benign prostate hyperplasia. *Glycobiology* **21,** 195–205 CrossRef Medline
67. Luo, C., Chen, S., Xu, N., Wang, C., Sai, W. B., Zhao, W., Li, Y. C., Hu, X. J., Tian, H., Gao, X. D., and Yao, W. B. (2017) Glycoengineering of pertuzumab and its impact on the pharmacokinetic/pharmacodynamic properties. *Sci. Rep.* **7,** 46347 CrossRef Medline
68. Satoh, M., Iida, S., and Shitara, K. (2006) Non-fucosylated therapeutic antibodies as next-generation therapeutic antibodies. *Expert Opin. Biol. Ther.* **6,** 1161–1173 CrossRef Medline
69. Bosmann, H. B., Hagopian, A., and Eylar, E. H. (1968) Glycoprotein biosynthesis: the characterization of two glycoprotein: fucosyl transferases in HeLa cells. *Arch Biochem. Biophys.* **128,** 470–481 CrossRef Medline
70. Ihara, H., Hanashima, S., Okada, T., Ito, R., Yamaguchi, Y., Taniguchi, N., and Ikeda, Y. (2010) Fucosylation of chitooligosaccharides by human α1,6-fucosyltransferase requires a nonreducing terminal chitotriose unit as a minimal structure. *Glycobiology* **20,** 1021–1033 CrossRef Medline
71. Ihara, H., Ikeda, Y., and Taniguchi, N. (2006) Reaction mechanism and substrate specificity for nucleotide sugar of mammalian α1,6-fucosyltransferase: a large-scale preparation and characterization of recombinant human FUT8. *Glycobiology* **16,** 333–342 CrossRef Medline
72. Kamińska, J., Glick, M. C., and Kościelak, J. (1998) Purification and characterization of GDP-L-Fuc:*N*-acetyl beta-D-glucosaminide alpha1→6-fucosyltransferase from human blood platelets. *Glycoconj. J.* **15,** 783–788 Medline
73. Longmore, G. D., and Schachter, H. (1982) Product-identification and substrate-specificity studies of the GDP-L-fucose:2-acetamido-2-deoxy-beta-D-glucoside (FUC goes to Asn-linked GlcNAc) 6-alpha-L-fucosyltransferase in a Golgi-rich fraction from porcine liver. *Carbohydr. Res.* **100,** 365–392 CrossRef Medline
74. Shao, M. C., Sokolik, C. W., and Wold, F. (1994) Specificity studies of the GDP-(L)-fucose: 2-acetamido-2-deoxy-beta-D-glucoside (Fuc→Asn-linked GlcNAc) 6-alpha-L-fucosyltransferase from rat-liver Golgi membranes. *Carbohydr. Res.* **251,** 163–173 CrossRef Medline
75. Voynow, J. A., Kaiser, R. S., Scanlin, T. F., and Glick, M. C. (1991) Purification and characterization of GDP-L-fucose-*N*-acetyl β-D-glucosaminide α1→6-fucosyltransferase from cultured human skin fibroblasts: requirement of a specific biantennary oligosaccharide as substrate. *J. Biol. Chem.* **266,** 21572–21577 Medline
76. Wilson, J. R., Williams, D., and Schachter, H. (1976) The control of glycoprotein synthesis: *N*-acetylglucosamine linkage to a mannose residue as a signal for the attachment of L-fucose to the asparagine-linked *N*-acetylglucosamine residue of glycopeptide from alpha1-acid glycoprotein. *Biochem. Biophys. Res. Commun.* **72,** 909–916 CrossRef Medline
77. Yang, Q., and Wang, L. X. (2016) Mammalian α-1,6-fucosyltransferase (FUT8) is the sole enzyme responsible for the *N*-acetylglucosaminyltransferase I-independent core fucosylation of high-mannose *N*-glycans. *J. Biol. Chem.* **291,** 11064–11071 CrossRef Medline
78. Yang, Q., Zhang, R., Cai, H., and Wang, L. X. (2017) Revisiting the substrate specificity of mammalian α1,6-fucosyltransferase reveals that it catalyzes core fucosylation of *N*-glycans lacking β1,3-arm GlcNAc. *J. Biol. Chem.* **292,** 14796–14803 CrossRef Medline
79. Calderon, A. D., Liu, Y., Li, X., Wang, X., Chen, X., Li, L., and Wang, P. G. (2016) Substrate specificity of FUT8 and chemoenzymatic synthesis of core-fucosylated asymmetric *N*-glycans. *Org. Biomol. Chem.* **14,** 4027–4031 CrossRef Medline
80. Li, L., Liu, Y., Ma, C., Qu, J., Calderon, A. D., Wu, B., Wei, N., Wang, X., Guo, Y., Xiao, Z., Song, J., Sugiarto, G., Li, Y., Yu, H., Chen, X., *et al.* (2015) Efficient chemoenzymatic synthesis of an *N*-glycan isomer library. *Chem. Sci.* **6,** 5652–5661 CrossRef Medline
81. Serna, S., Yan, S., Martin-Lomas, M., Wilson, I. B., and Reichardt, N. C. (2011) Fucosyltransferases as synthetic tools: glycan array based substrate selection and core fucosylation of synthetic *N*-glycans. *J. Am. Chem. Soc.* **133,** 16495–16502 CrossRef Medline
82. Tseng, T. H., Lin, T. W., Chen, C. Y., Chen, C. H., Lin, J. L., Hsu, T. L., and Wong, C. H. (2017) Substrate preference and interplay of fucosyltransferase 8 and *N*-acetylglucosaminyltransferases. *J. Am. Chem. Soc.* **139,** 9431–9434 CrossRef Medline
83. Moremen, K. W., Ramiah, A., Stuart, M., Steel, J., Meng, L., Forouhar, F., Moniz, H. A., Gahlay, G., Gao, Z., Chapla, D., Wang, S., Yang, J. Y., Prabhakar, P. K., Johnson, R., Rosa, M. D., *et al.* (2018) Expression system for structural and functional studies of human glycosylation enzymes. *Nat. Chem. Biol.* **14,** 156–162 CrossRef Medline
84. Yang, Q., An, Y., Zhu, S., Zhang, R., Loke, C. M., Cipollo, J. F., and Wang, L. X. (2017) Glycan remodeling of human erythropoietin (EPO) through combined mammalian cell engineering and chemoenzymatic transglycosylation. *ACS Chem. Biol.* **12,** 1665–1673 CrossRef Medline
85. Kadirvelraj, R., Yang, J. Y., Sanders, J. H., Liu, L., Ramiah, A., Prabhakar, P. K., Boons, G. J., Wood, Z. A., and Moremen, K. W. (2018) Human *N*-acetylglucosaminyltransferase II substrate recognition uses a modular architecture that includes a convergent exosite. *Proc. Natl. Acad. Sci. U.S.A.* **115,** 4637–4642 CrossRef Medline
86. Meng, L., Forouhar, F., Thieker, D., Gao, Z., Ramiah, A., Moniz, H., Xiang, Y., Seetharaman, J., Milaninia, S., Su, M., Bridger, R., Veillon, L., Azadi, P., Kornhaber, G., Wells, L., *et al.* (2013) Enzymatic basis for *N*-glycan sialylation: structure of rat α2,6-sialyltransferase (ST6GAL1) reveals conserved and unique features for glycan sialylation. *J. Biol. Chem.* **288,** 34680–34698 CrossRef Medline
87. Ihara, H., Okada, T., Taniguchi, N., and Ikeda, Y. (2020) Involvement of the alpha-helical and Src homology 3 domains in the molecular assembly and enzymatic activity of human α1,6-fucosyltransferase, FUT8. *Biochim. Biophys. Acta* **1864,** 129596 CrossRef Medline
88. Krissinel, E., and Henrick, K. (2007) Inference of macromolecular assemblies from crystalline state. *J. Mol. Biol.* **372,** 774–797 CrossRef Medline
89. Pratap, J. V., Luisi, B. F., and Calladine, C. R. (2013) Geometric principles in the assembly of α-helical bundles. *Philos. Trans. A Math. Phys. Eng. Sci.* **371,** 20120369 CrossRef Medline
90. Desrochers, G., Cappadocia, L., Lussier-Price, M., Ton, A. T., Ayoubi, R., Serohijos, A., Omichinski, J. G., and Angers, A. (2017) Molecular basis of interactions between SH3 domain-containing proteins and the proline-rich region of the ubiquitin ligase Itch. *J. Biol. Chem.* **292,** 6325–6338 CrossRef Medline
91. Paulson, J. C., and Colley, K. J. (1989) Glycosyltransferases: structure, localization, and control of cell type-specific glycosylation. *J. Biol. Chem.* **264,** 17615–17618 Medline
92. Jones, D. T., and Cozzetto, D. (2015) DISOPRED3: precise disordered region predictions with annotated protein-binding activity. *Bioinformatics* **31,** 857–863 CrossRef Medline
93. Tomida, S., Takata, M., Hirata, T., Nagae, M., Nakano, M., and Kizuka, Y. (2020) The SH3 domain in the fucosyltransferase FUT8 controls FUT8 activity and localization and is essential for core fucosylation. *J. Biol. Chem.* **295,** 7992–8004 CrossRef Medline

94. Oriol, R., Mollicone, R., Cailleau, A., Balanzino, L., and Breton, C. (1999) Divergent evolution of fucosyltransferase genes from vertebrates, invertebrates, and bacteria. *Glycobiology* **9,** 323–334 CrossRef Medline
95. Martinez-Duncker, I., Mollicone, R., Candelier, J. J., Breton, C., and Oriol, R. (2003) A new superfamily of protein-O-fucosyltransferases, alpha2-fucosyltransferases, and alpha6-fucosyltransferases: phylogeny and identification of conserved peptide motifs. *Glycobiology* **13,** 1C–5C CrossRef Medline
96. Brzezinski, K., Stepkowski, T., Panjikar, S., Bujacz, G., and Jaskolski, M. (2007) High-resolution structure of NodZ fucosyltransferase involved in the biosynthesis of the nodulation factor. *Acta Biochim. Pol.* **54,** 537–549 CrossRef Medline
97. Pei, J., Kim, B. H., and Grishin, N. V. (2008) PROMALS3D: a tool for multiple protein sequence and structure alignments. *Nucleic Acids Res.* **36,** 2295–2300 CrossRef Medline
98. Liu, D., Gao, Z., and Yue, L. (2019) Fucosyltransferase 8 deficiency suppresses breast cancer cell migration by interference of the FAK/integrin pathway. *Cancer Biomark* **25,** 303–311 CrossRef Medline
99. Shinkawa, T., Nakamura, K., Yamane, N., Shoji-Hosaka, E., Kanda, Y., Sakurada, M., Uchida, K., Anazawa, H., Satoh, M., Yamasaki, M., Hanai, N., and Shitara, K. (2003) The absence of fucose but not the presence of galactose or bisecting *N*-acetylglucosamine of human IgG1 complex-type oligosaccharides shows the critical role of enhancing antibody-dependent cellular cytotoxicity. *J. Biol. Chem.* **278,** 3466–3473 CrossRef Medline
100. Crispin, M., Harvey, D. J., Chang, V. T., Yu, C., Aricescu, A. R., Jones, E. Y., Davis, S. J., Dwek, R. A., and Rudd, P. M. (2006) Inhibition of hybrid- and complex-type glycosylation reveals the presence of the GlcNAc transferase I-independent fucosylation pathway. *Glycobiology* **16,** 748–756 CrossRef Medline
101. Breton, C., Oriol, R., and Imberty, A. (1998) Conserved structural features in eukaryotic and prokaryotic fucosyltransferases. *Glycobiology* **8,** 87–94 CrossRef Medline
102. Taujale, R., Venkat, A., Huang, L. C., Zhou, Z., Yeung, W., Rasheed, K. M., Li, S., Edison, A. S., Moremen, K. W., and Kannan, N. (2020) Deep evolutionary analysis reveals the design principles of fold A glycosyltransferases. *Elife* **9,** e54532 CrossRef Medline
103. Kadirvelraj, R., Yang, J. Y., Sanders, J. H., Liu, L., Ramiah, A., Prabhakar, P. K., Boons, G. J., Wood, Z. A., and Moremen, K. W. (2018) Human *N*-acetylglucosaminyltransferase II substrate recognition uses a modular architecture that includes a convergent exosite. *Proc. Natl. Acad. Sci. U.S.A.* **115,** 4637–4642 Medline
104. Li, T., Liu, L., Wei, N., Yang, J. Y., Chapla, D. G., Moremen, K. W., and Boons, G. J. (2019) An automated platform for the enzyme-mediated assembly of complex oligosaccharides. *Nat. Chem.* **11,** 229–236 CrossRef Medline
105. Liu, L., Prudden, A. R., Capicciotti, C. J., Bosman, G. P., Yang, J. Y., Chapla, D. G., Moremen, K. W., and Boons, G. J. (2019) Streamlining the chemoenzymatic synthesis of complex *N*-glycans by a stop and go strategy. *Nat. Chem.* **11,** 161–169 CrossRef Medline
106. Liu, L., Prudden, A. R., Bosman, G. P., and Boons, G. J. (2017) Improved isolation and characterization procedure of sialylglycopeptide from egg yolk powder. *Carbohydr. Res.* **452,** 122–128 CrossRef Medline
107. van den Eijnden, D. H., Blanken, W. M., and van Vliet, A. (1986) Branch specificity of beta-D-galactosidase from *Escherichia coli*. *Carbohydr. Res.* **151,** 329–335 CrossRef Medline
108. Trastoy, B., Du, J. J., Klontz, E. H., Li, C., Cifuente, J. O., Wang, L. X., Sundberg, E. J., and Guerin, M. E. (2020) Structural basis of mammalian high-mannose *N*-glycan processing by human gut Bacteroides. *Nat. Commun.* **11,** 899 CrossRef Medline
109. Kabsch, W. (2010) Xds. *Acta Crystallogr. D Biol. Crystallogr.* **66,** 125–132 CrossRef Medline
110. Adams, P. D., Afonine, P. V., Bunkoczi, G., Chen, V. B., Davis, I. W., Echols, N., Headd, J. J., Hung, L. W., Kapral, G. J., Grosse-Kunstleve, R. W., McCoy, A. J., Moriarty, N. W., Oeffner, R., Read, R. J., Richardson, D. C., *et al.* (2010) PHENIX: a comprehensive Python-based system for macromolecular structure solution. *Acta Crystallogr. D Biol. Crystallogr.* **66,** 213–221 CrossRef Medline
111. Emsley, P., Lohkamp, B., Scott, W. G., and Cowtan, K. (2010) Features and development of Coot. *Acta Crystallogr. D Biol. Crystallogr.* **66,** 486–501 CrossRef Medline
112. Urzhumtsev, A., Afonine, P. V., and Adams, P. D. (2013) TLS from fundamentals to practice. *Crystallogr. Rev.* **19,** 230–270 CrossRef Medline
113. Agirre, J., Iglesias-Fernández, J., Rovira, C., Davies, G. J., Wilson, K. S., and Cowtan, K. D. (2015) Privateer: software for the conformational validation of carbohydrate structures. *Nat. Struct. Mol. Biol.* **22,** 833–834 CrossRef Medline
114. Lutteke, T., Frank, M., and von der Lieth, C. W. (2004) Carbohydrate Structure Suite (CSS): analysis of carbohydrate 3D structures derived from the PDB. *Nucleic Acids Res.* **33,** D242–D246 CrossRef Medline
115. Liebschner, D., Afonine, P. V., Moriarty, N. W., Poon, B. K., Sobolev, O. V., Terwilliger, T. C., and Adams, P. D. (2017) Polder maps: improving OMIT maps by excluding bulk solvent. *Acta Crystallogr. D Struct. Biol.* **73,** 148–157 CrossRef Medline
116. Neelamegham, S., Aoki-Kinoshita, K., Bolton, E., Frank, M., Lisacek, F., Lütteke, T., O'Boyle, N., Packer, N. H., Stanley, P., Toukach, P., Varki, A., and Woods, R. J., SNFG Discussion Group (2019) Updates to the symbol nomenclature for glycans guidelines. *Glycobiology* **29,** 620–624 CrossRef Medline
117. Wallace, A. C., Laskowski, R. A., and Thornton, J. M. (1995) LIGPLOT: a program to generate schematic diagrams of protein-ligand interactions. *Protein Eng.* **8,** 127–134 CrossRef Medline
118. Diederichs, K., and Karplus, P. A. (1997) Improved R-factors for diffraction data analysis in macromolecular crystallography. *Nat. Struct. Biol.* **4,** 269–275 CrossRef Medline